

Student thesis series INES nr 549

Development of a deep learning method for soil moisture estimation at high spatial and temporal resolution using satellite data

Nicklas Thorlund Simonsen

2021

Department of
Physical Geography and Ecosystem Science
Lund University
Sölvegatan 12
S-223 62 Lund
Sweden



Nicklas Thorlund Simonsen (2021).

Development of a deep learning method for soil moisture estimation at high spatial and temporal resolution using satellite data

Master degree thesis, 30 credits in *Geomatics*

Department of Physical Geography and Ecosystem Science, Lund University

Level: Master of Science (MSc)

Course duration: *January* 2021 until *June* 2021

Disclaimer

This document describes work undertaken as part of a program of study at the University of Lund. All views and opinions expressed herein remain the sole responsibility of the author, and do not necessarily represent those of the institute.

Development of a deep learning method for soil moisture estimation at high spatial and temporal resolution using satellite data

Nicklas Thorlund Simonsen

Master thesis, 30 credits, in *Geomatics*

Supervisor

Zheng Duan, Associate professor

Department of Physical Geography and Ecosystem Science, Lund University

Exam committee

Wenxin Zhang, Researcher

Department of Physical Geography and Ecosystem Science, Lund University

Babak Mohammadi, Doctoral student

Department of Physical Geography and Ecosystem Science, Lund University

Acknowledgements

I would like to express my gratitude to Zheng Duan who supervised me through this thesis. He has been a pillar of support throughout this process and has been forthcoming to any questions I have posed. I sincerely appreciate the efforts he has put into reviewing this thesis thoroughly and critically, especially during critical periods leading up to deadlines.

I would also like to extend my gratitude to Wenxin Zhang, who has been acting examiner and reviewing my submissions. His critical feedback and attention to detail has helped shape the quality of this thesis.

The soil moisture measurements at the ICOS stations were made available by Jutta Holst at the Department of Physical Geography and Ecosystem Science, Lund University. This data will also be available at the ICOS Carbon Portal at <https://www.icos-cp.eu/observations/carbon-portal>

Abstract

Soil moisture (SM) is an essential climate variable that controls fundamental hydrological and climatic processes. Soil moisture products derived from microwave remote sensing often provide measurements at low spatial resolution and incomplete temporal records. This thesis presents a novel method for estimation soil moisture at both high spatial and temporal resolution by using a deep learning recurrent neural network model. The model relies primarily on Sentinel-1 synthetic aperture radar data but includes additional ancillary data, such as Sentinel-2 vegetation indices, land cover, and weather variables. The model is calibrated and validated on four SM probe networks within continental Europe with data from the International Soil Moisture Network (ISMN) and the Integrated Carbon Observation System (ICOS). The model has been compared with existing SM products and has shown comparable or better results with a mean absolute error of 9.33% and a correlation of $r=0.49$ with observed measurements. It performs best over agricultural land covers in temperate regions, where satellite observations are most frequent, and poorer over vegetated land surfaces like forests due to the attenuation of microwave signals. The temporal predictions show high accuracy and precision, while the spatial predictions retain a high accuracy but with lower precision. The predictions show satisfactory results overall but warrant further research to test the feasibility of this architecture over larger areas and different climate types.

Table of Contents

Acknowledgements.....	ii
Abstract.....	iii
Nomenclature.....	vi
1. Introduction.....	1
1.1. Microwave remote sensing of soil moisture	1
1.2. Machine learning and deep learning	3
1.3. Aim and objectives of this thesis	4
2. Background.....	4
3. Methodology	6
3.1. Study areas	6
3.1.1. Climate.....	6
3.1.2. Topography	7
3.1.3. Land cover	8
3.2. Data.....	9
3.2.1. In situ measurements of soil moisture and soil temperature.....	9
3.2.2. Sentinel-1 data	10
3.2.3. Sentinel-2 data	11
3.2.4. Meteorological data	13
3.2.5. Topographic and land cover data.....	13
3.2.6. Evaluation of intervariable relationships	13
3.3. Deep learning model	14
3.3.1. Model architecture	14
3.3.2. Model hyperparameters	17
3.3.3. Evaluation metrics	20
3.3.4. Performance of model variations	20
3.3.5. Evaluation against existing soil moisture products.....	20
4. Results.....	22
4.1. Statistical relationships of model variables.....	22
4.1.1. Linear correlations	22
4.1.2. Normalized distributions.....	23
4.1.3. Sigma Nought backscatter and vegetation index feature distributions.....	26
4.1.4. Time-series analysis.....	28

4.2. Model results.....	29
4.2.1. Evaluation of land cover and region wide model results.....	29
4.2.2. Comparison with existing SM products.....	31
4.2.3. Spatial and temporal model predictions.....	34
5. Discussion.....	36
5.1. Evaluation of existing products	36
5.2. Deep learning model.....	36
5.3. Ancillary predictive variables	38
5.4. Soil moisture variations by land cover and region.....	39
5.5. Critical reflections on the accuracy of surface soil moisture	40
5.6. Future work.....	40
6. Conclusions.....	41
References.....	43
Appendix A: Data specifications	51
Appendix B: Model and Soil Moisture Products Predictions.....	54

Nomenclature

Abbreviation	Meaning
Adam	Adaptive Moment Estimation
AEMET	State Meteorological Agency
AMSR-E	Advanced Microwave Scanning Radiometer - Earth Observing System
ANN	Artificial Neural Network
AOT	Aerosol Optical Thickness
AVHRR	Advanced Very-High-Resolution Radiometer
BOA	Bottom Of Atmosphere
CIALE	Centro Hispano Luso de Investigaciones Agrarias Universidad de Salamanca
CLC	CORINE Land Cover 2018
CLR	Cyclical Learning Rate
CNN	Convolutional Neural Network
CSM	Copernicus Soil Moisture
DDV	Dense Dark Vegetation [algorithm]
DEM	Digital Elevation Model
DL	Deep Learning
DLM	Deep Learning Model
$DLM_{agriculture}$	Agriculture Deep Learning Model
DLM_{full}	Full Deep Learning Model
$DLM_{minimum}$	Minimum Parameter Deep Learning Model
DMI	Danish Meteorological Institute
DTM	Digital Terrain Model
ECV_SM	Essential Climate Variables for Soil Moisture
ESA	European Space Agency
FAO	Food and Agriculture Organization
FMI	Finnish Meteorological Institute
GRD	Ground Range Detected
GSD	Ground Sampling Distance
HH	Horizontal-Horizontal [polarization]
HOBE	The Danish Hydrological Observatory
HV	Horizontal-Vertical [polarization]
HWSD	Harmonized World Soil Database 1.2
ICOS	Integrated Carbon Observation System
IGN	Instituto Geográfico Nacional
ISMN	International Soil Moisture Network

LUT	Look Up Table
MAE	Mean Absolute Error
NASA	National Aeronautics and Space Administration
NDVI	Normalized Difference Vegetation Index
NDWI	Normalized Difference Water Index
NLS	National Land Survey of Finland
NN	Neural Network
RNN	Recurrent Neural Network
SAR	Synthetic Aperture Radar
SDFE	Styrelsen for Dataforsyning og Effektivisering
SM	Soil moisture
SMAP	Soil Moisture Active Passive
SMHI	The Swedish Meteorological and Hydrological Institute
SMOS	Soil Moisture and Ocean Salinity
SNAP	Sentinel Application Platform
SSM	Surface soil moisture
TA	Air temperature
TA_{max}	Maximum Daily Air Temperature
TA_{mean}	Mean Daily Air Temperature
TA_{min}	Minimum Daily Air Temperature
TIROS-N	Television and Infrared Observation Satellite
TOA	Top Of Atmosphere
TS	Soil temperature
TS_{max}	Maximum Daily Soil Temperature
VH	Vertical-Horizontal [polarization]
VI	Vegetation Index
VV	Vertical-Vertical [polarization]
σ^0	Sigma Nought backscatter

This page has been left intentionally blank

1. Introduction

Soil moisture (SM) is an essential climate variable that controls fundamental hydrological and climatic processes such as infiltration, runoff, and evapotranspiration (Wang and Qu 2009; Babaeian et al. 2018; Abowarda et al. 2021). Surface soil moisture (SSM) controls the latent and sensible heat fluxes at the ground with the atmosphere, thus linking the water and energy balance through the moisture and temperature of the soil (Robock et al. 2000). It has a significant influence on the agronomic, biological, ecological, and hydrological behavior of the soil mass (Susha Lekshmi et al. 2014). Hereunder applications concerning topics like precision agriculture, erosion-, climate- and runoff modelling, and flood forecasting (Peng et al. 2020). Many of these applications require high accuracy at a high spatial resolution, such as precision agriculture for better water management. Traditionally, field-based measurements of SM have been limited to in situ recordings using SM probes (Wang et al. 2012). This approach provides a high temporal resolution of data but lacks the spatial component without implementing a grid of SM probes, which is a resource intensive operation. Globally, there is a lack of in situ SM probes with historical overlap for testing models and validating results. Several data hosting facilities, such as the International Soil Moisture Network (ISMN) (Dorigo et al. 2011; Dorigo et al. 2013) has aimed to improve this by creating a collective global dataset. Unfortunately, many of the SM probes are no longer operational and thus the global overlap of in situ data is still very small. Remote sensing has provided solutions to scale up these measurements with both global and historic SM estimates (Dorigo et al. 2015). However, remote sensing-based solutions for SM are limited to temporal resolutions ranging from days to several weeks. Moreover, higher temporal resolutions often result in a decrease in spatial resolution or coverage. Both of these limitations make remote sensing an unviable options, where both high temporal and spatial resolution is necessary (Zhang and Zhou 2016).

1.1. Microwave remote sensing of soil moisture

Remotely sensed SM estimations are most often based on microwave radar (Njoku and Kong 1977; Schmugge 1978; Jackson 1993; Njoku et al. 2003; Liu et al. 2011) or optical images with emphasis on the infrared spectrum (Rahimzadeh-Bajgirani et al. 2013; El Hajj et al. 2017; Sadeghi et al. 2017). Microwaves are able to capture variations in SSM due to the large difference in dielectric constant between dry and wet soil (Schmugge 1978; Engman et al. 1995; Owe and Van De Griend 1998) and can penetrate light vegetation (Njoku et al. 2003; Wagner et al. 2003; Abowarda et al. 2021) and cloud cover (Park et al. 2019). Moreover, microwave remote sensing is not dependent on solar reflectance and can thus operate at both day and night. For these reasons microwave radar sensors are often used in global monitoring missions such as the Soil Moisture and Ocean Salinity (SMOS), Soil Moisture Active Passive (SMAP), and Advanced Microwave Scanning Radiometer - Earth Observing System (AMSR-E) (Kerr et al. 2001; Njoku et al. 2003; Entekhabi et al. 2015). The estimation of SM from microwave radar relies on the assumption that the only major change to the soil over short periods is the SM. This is because the backscatter coefficient measured by the radar is also highly sensitive to changes in surface roughness, which often occurs over longer periods.

Sensors focusing on SM are often passive and measure the brightness temperature of the surface and thus require large fields of view to detect enough energy to record a signal. Hence,

spatial resolutions are in the range of 25-60 km for most of these sensors. Active sensors emit their own energy and measure the backscatter coefficient from the surface and can do so at higher spatial resolution than passive sensors. However, active sensors are more sensitive to noise in the signals (Das et al. 2019) and higher spatial resolutions are compromised by lower temporal resolutions. Additionally, higher spatial resolution sensors are also likely to be more affected by changes in surface roughness as these changes frequently occur over small areas and short periods. The size of the antenna used to measure the backscatter is proportional to the spatial resolution achieved with the microwave radar. Hence, high spatial resolution data is unfeasible for traditional beam-scanning radars, which necessitates the application of synthetic aperture radars (SAR). SAR uses the motion of the antenna to create spatial resolutions higher than what can be achieved by conventional radars of similar size. SAR is an active sensor emitting its own energy and the backscatter coefficient is expressed as Sigma nought (σ^0).

Repeat cycles and spatial resolutions for the satellites carrying the microwave sensors range from 2-60 days and 0.01-156 km, respectively (Mohanty et al. 2017). Efforts have been made to combine the two types of sensors into a single product, such as Essential Climate Variables for Soil Moisture (ECV_SM), (Liu et al. 2011; Dorigo et al. 2015; Dorigo et al. 2017) and utilizing the advantages of both. Microwave signals at higher spatial resolution are increasingly susceptible to radiometric interference from surface roughness (Moran et al. 2000; Lievens et al. 2011), vegetation (Jackson et al. 1996; Le Hégarat-Masclé et al. 2002; Dorigo et al. 2017), and heterogeneity in land cover (Wagner et al. 2003), hence why most SSM specific radar missions focus on lower spatial resolution capture. Multiple studies have used downscaling methods with ancillary predictors such as topography, soil texture, and vegetation (Lievens et al. 2011; Prakash et al. 2012; Ranney et al. 2015; Abowarda et al. 2021), optical imagery (Hassan-Esfahani et al. 2015; Sadeghi et al. 2017) or both (Rahimzadeh-Bajgirani et al. 2013; He et al. 2014; Gao et al. 2017; El Hajj et al. 2017; Peng et al. 2020) to achieve high-resolution results, while bypassing the limitations of high-resolution microwave satellites. However, these approaches introduce new limitations of data availability as they rely on overlapping coverage of multiple sensors.

Sentinel-1 is currently one of the most advanced SAR mission that supports systematic capture of SSM (Peng et al. 2020) at high spatial and temporal resolution. It consists of two satellites in sun-synchronous orbit with an average combined repeat cycle of 6 days globally, but down to 1 day in some regions. The Sentinel-1 SAR uses four different polarizations in C-band: Vertical-Vertical (VV), Horizontal-Horizontal (HH), or combinations between the two, VH and HH. However, publicly available data from Sentinel-1 is limited to VV and VH polarizations. Each polarization captures a different type of surface information depending on the electrical and geometric properties of the surface (Baghdadi et al. 2006). For SSM studies using SAR, some (Baghdadi et al. 2016; El Hajj et al. 2016) use HH/HV polarizations, while others (Gao et al. 2017; El Hajj et al. 2017) rely on VV/VH polarizations, or both (Paloscia et al. 2013). Regarding the most suitable polarizations, the results from the studies are inconclusive and appear region and sensor specific. The Sentinel-1 mission has been used in multiple SM studies (Balenzano et al. 2011; Paloscia et al. 2013; Gao et al. 2017; El Hajj et al. 2017; Singh et al. 2020) including a publicly available SM dataset, Copernicus Soil Moisture (CSM), covering continental Europe. The CSM uses an empirical model (Bauer-

Marschallinger et al. 2019) that scales the backscatter coefficient based on historical lows and highs to derive SM from the SAR images.

1.2. Machine learning and deep learning

Artificial intelligence (AI) has been a subject of exploration since the 1950s (Chollet 2018), when researchers challenged the idea of “thinking” computers. Since then, the sub-categories under the umbrella of AI have increased exponentially, hereunder machine learning (ML) and the more advanced branch of it, deep learning (DL). ML arises from a paradigm shift in classic programming theory, where rules and data produce answers, whereas ML attempts to find rules based on data and answers. Hence, the algorithm is taught what to expect and finds statistical structures in these relationships that allows it to “learn” a set of rules to interpret new data. Artificial Neural Networks (ANN) consist of a collection of connected units and loosely model the neuron connections in the biological brain (McCulloch and Pitts 1943; Géron 2019). They are a specialization of ML that excels at deriving complex relationship from large datasets through weights and step functions (Rosenblatt 1958). ANNs are based on layers of relatively simple mathematical transformations, which are stacked to increase the level of complexity they can derive from the data. Hence, ANNs are often used in remote sensing-based SM studies (Paloscia et al. 2013; Baghdadi et al. 2016; El Hajj et al. 2016; Alexakis et al. 2017) that use large multivariate datasets. However, once a datum is ingested into the model it becomes increasingly modified as it passes through the layers and transformations. This makes ANNs less suitable for time-series, where antecedent conditions hold important information about current and future events.

DL is a specific subfield of machine learning that emphasizes successive layers in a model (Chollet 2018). These layers are used to extract increasingly meaningful and complex data from data that regular (shallow) ML models are unable to. These layers are most often represented in Neural Networks (NN) structured as sequences of layers. Convolutional Neural Networks (CNN) are perhaps the best-known DL variants of the traditional ANN within remote sensing because they focus on 2-dimensional representations, or images. CNNs are constructed of several convolutions of various sizes, that iterate through the data in a moving window. Each window, or convolution, extract conceptual shapes or patterns from the image, with smaller convolutions focusing on more detailed features. They can thus mimic how humans perceive 2-dimensional objects by reconstructing these features in a hierarchy of details. The Recurrent Neural Networks (RNN) are a DL variant of the traditional ANN that specialize in sequential data, such as time-series. RNNs use cell states to pass information along the layers without modifications, thus allowing the network to hold onto information until it is needed. RNNs have seen some applications within remote sensing-based SM studies in recent years. A study by Su et al. (2019) used this architecture for anomaly detection of various time-series, including SMAP SM data. While this study is not concerned with remote sensing analysis but rather the structure of the data used, it shows the feasibility of RNNs on satellite data. Additionally, Masrur Ahmed et al. (2021) applied a combined RNN-CNN structure to forecast SM data from a combined in situ/remote sensing dataset over south-eastern Australia. RNNs have not been applied directly for SM estimation and hence this thesis provides a fundamental investigation into its suitability for this type of analysis.

1.3. Aim and objectives of this thesis

The aim of this thesis is to develop and evaluate a deep learning-based method to estimate SSM at high spatial and temporal resolution across multiple land cover and climate types.

Specifically, the objectives of this study are to:

- 1) Develop a model based on RNNs to estimate SSM from Sentinel-1 SAR data by using ancillary information from Sentinel-2 optical imagery, meteorological, and topographic data. The model is then calibrated and validated on in situ data collected from SM probes.
- 2) Build a pipeline structure that automates the processing and harmonizing of the multivariate input, trains the model, and creates an SM prediction.
- 3) Evaluate the model against existing global and regional SM products based on various satellites to determine its feasibility as a competitive solution.

2. Background

Estimations of SM from remote sensing date back to 1978 with the launch of the Advanced Very-High-Resolution Radiometer (AVHRR) sensor aboard the Television and Infrared Observation Satellite (TIROS-N) satellite and has since grown to encompass multiple wavelength from different sensor types at various spatial and temporal resolutions (Kerr et al. 2001; Njoku et al. 2003; Wang and Qu 2009; Entekhabi et al. 2015; Mohanty et al. 2017; Peng et al. 2020). The wavelengths utilized by the microwave radars are generally limited to the L- (1.0-2.0 GHz), C- (4.0-8.0 GHz), and X- (8.0-12.0 GHz) band in order of low to high frequency at decreasing soil penetration capabilities. Because of the high penetration capability of the L-band (Owe and Van De Griend 1998), it is the most suitable for SM observation (Boisvert et al. 1995; Mohanty et al. 2017; El Hajj et al. 2019). However, due to the multi-purpose nature of most satellites and the complicated structures required to transmit and receive microwaves at low frequencies, only few sensors operate in the L-band at the time of writing, and most do so at low spatial resolution (>25 km). The second-best option is the C-band microwaves, which have a penetration depth between 1-6 cm (Owe and Van De Griend 1998; Koyama et al. 2017). The Sentinel-1 mission is, despite its limitation of C-band microwaves, one of the most widely used sensors in SM studies since its launch. It has been used by NASA to downscale the SMAP data to 3 km and 1 km resolutions (Das et al. 2019) and ASCAT for 1 km resolution products (Bauer-Marschallinger et al. 2018). The Sentinel-1 mission is currently in its early stages with just five years of available data and is thus not suitable for climate models, that rely on longer time-series (Peng et al. 2020). However, the Sentinel-1 mission is planned to continue for the next decades under the Copernicus programme and will be an important data source going forwards.

SSM is a complex hydrological and ecological variable affected by both precipitation, soil texture, topography, temperature, and vegetation (Seneviratne et al. 2010; Wang et al. 2012; Ke et al. 2016; Abbaszadeh et al. 2019). Hence why studies have used a Normalized Difference Vegetation Index (NDVI) (Ahmad et al. 2010; Paloscia et al. 2013; Gao et al. 2017; Sadeghi et al. 2017; Babaeian et al. 2018; Abowarda et al. 2021), soil texture (Mittelbach et al. 2012; Ranney et al. 2015; Abowarda et al. 2021), land-surface temperature (Sadeghi et al. 2017; Adeyemi et al. 2018; Abowarda et al. 2021), and precipitation (Adeyemi et al. 2018; Abowarda

et al. 2021) either as an ancillary predictor with microwave-based remote sensing or as a standalone index. Moreover, a study by Chang and Islam (2000) showed that it was possible to reverse the relationship and infer soil texture from microwave-based SM data. Some studies (Abbaszadeh et al. 2019; Wei et al. 2019) have applied all of the above ancillary predictors and more using decision tree machine learning approaches. The studies, however, are concerned with the downscaling of SMAP data to 1 km spatial resolution, which is still an order of magnitude above field-scale estimations.

ML has primarily been applied in remotely sensed SM studies as a method to downscale microwave radars with low spatial resolution by utilizing both high spatial resolution microwave radars and optical imagery (Ahmad et al. 2010; Ali et al. 2015; Im et al. 2016; Hu et al. 2018; Abowarda et al. 2021). These methods often rely on Support Vector Machines and Random Forest, which are shallow in nature and often inadequate in capturing the complex relationship in multivariate datasets. Some studies have also applied ANNs to SM estimations from remote sensing (Baghdadi et al. 2012; Paloscia et al. 2013; Hassan-Esfahani et al. 2015; Xing et al. 2017) and generally show better performance than traditional machine learning approaches (Notarnicola et al. 2008; Ali et al. 2015). Relatively few studies (Adeyemi et al. 2018; Hu et al. 2018; Wang et al. 2018; Ma et al. 2019) use DL NNs at the time of writing and are mostly limited to CNNs. RNNs have seen limited use within remote sensing (Ma et al. 2019; Wang et al. 2019; Qi et al. 2020) and have been previously applied most widely to fields of language and speech recognition and generation (Murakami and Taguchi 1991; Medsker et al. 2001; Mikolov et al. 2010) with few other widespread uses. In recent years RNNs have seen a surge in interest outside the fields of origin and have been used for anomaly detection of time-series (Su et al. 2019), time-series classification and forecasting (Malhotra et al. 2017), and prediction of missing values in time-series (Che et al. 2018). Additionally, several studies have combined CNNs and RNNs to produce networks for spatio-temporal predictions (Liang and Hu 2015; Visin et al. 2015; Pelletier et al. 2019; Wan et al. 2019; Hewage et al. 2020). The surge in popularity is a result of several factors (Chollet 2018; Géron 2019): The availability of processing power, the development of high-level assembly libraries, and the increase in data availability. Especially the latter point has been experienced in the remote sensing field with a rapid increase in commercial satellites every year. Because of this, it is very likely that DL will continue to grow in popularity in the field of earth observation and SM estimation.

3. Methodology

3.1. Study areas

3.1.1. Climate

The study areas span four European countries: Denmark, Finland, Spain, and Sweden (Fig. 1) and are, except Sweden, composed of clusters of SM probes. The probes in Sweden are located at discrete locations throughout the country. Table 1 describes the extent of each site, the name of the probe network, the type of probe used, and the total number of probes in the network. The total area covering the probes in Sweden correspond to the size and number of pixels required by the Sentinel-1 images to capture each area. The study period is between 2016-09-20 and 2019-02-19, or 883 days, with most probes supplying a near-complete record during this time.

Table 1. Geographic and technical information about the SM probes used for calibration and validation of the model. Probe networks are abbreviated as The Danish Hydrological Institute (HOBE), Finnish Meteorological Institute (FMI), Centro Hispano Luso de Investigaciones Agrarias Universidad de Salamanca (CIALE responsible for REMEDHUS), and the Integrated Carbon Observation System (ICOS).

Region	Total area (minimum bounding geometry)	Probe network name	Probe type(s)	Number of probes
Denmark	889 km ²	HOBE	Decagon 5TE	28
Finland	415 km ²	FMI	Decagon 5TE CS655	8
Spain	1343 km ²	REMEDHUS	Stevens Hydra Probe	20
Sweden	5 x 10m ²	ICOS	ThetaProbe ML2, Campbell Thermocouple, Type E	5

The Spanish site (41.31N, 5.41W) is a cold semi-arid climate (Peel et al. 2007) with an annual precipitation of less than 400 mm and mean annual temperature between 10-12.5 °C (State Meteorological Agency 2021). The Danish site (55.96N, 9.09E) is a warm-summer humid continental climate (Peel et al. 2007) with an annual precipitation of 750 mm and mean annual temperature of 7.7 °C (Danish Meteorological Institute 2016). The Swedish sites cover two climate types from warm-summer humid continental in the south to subarctic in the north (Peel et al. 2007). The precipitation at these sites ranges from 500-900 mm annually and decreases from south to north (Swedish Meteorological and Hydrological Institute 2021a). The temperature follows a similar south-to-north pattern with an annual mean of 8-10°C in the south and -3-(-2)°C in the north (Swedish Meteorological and Hydrological Institute 2021b). The Finnish site (67.27N, 26.67E) is a subarctic climate (Peel et al. 2007) with an annual precipitation of less than 600 mm and mean annual temperature of -0.6 °C (Finnish Meteorological Institute 2021).

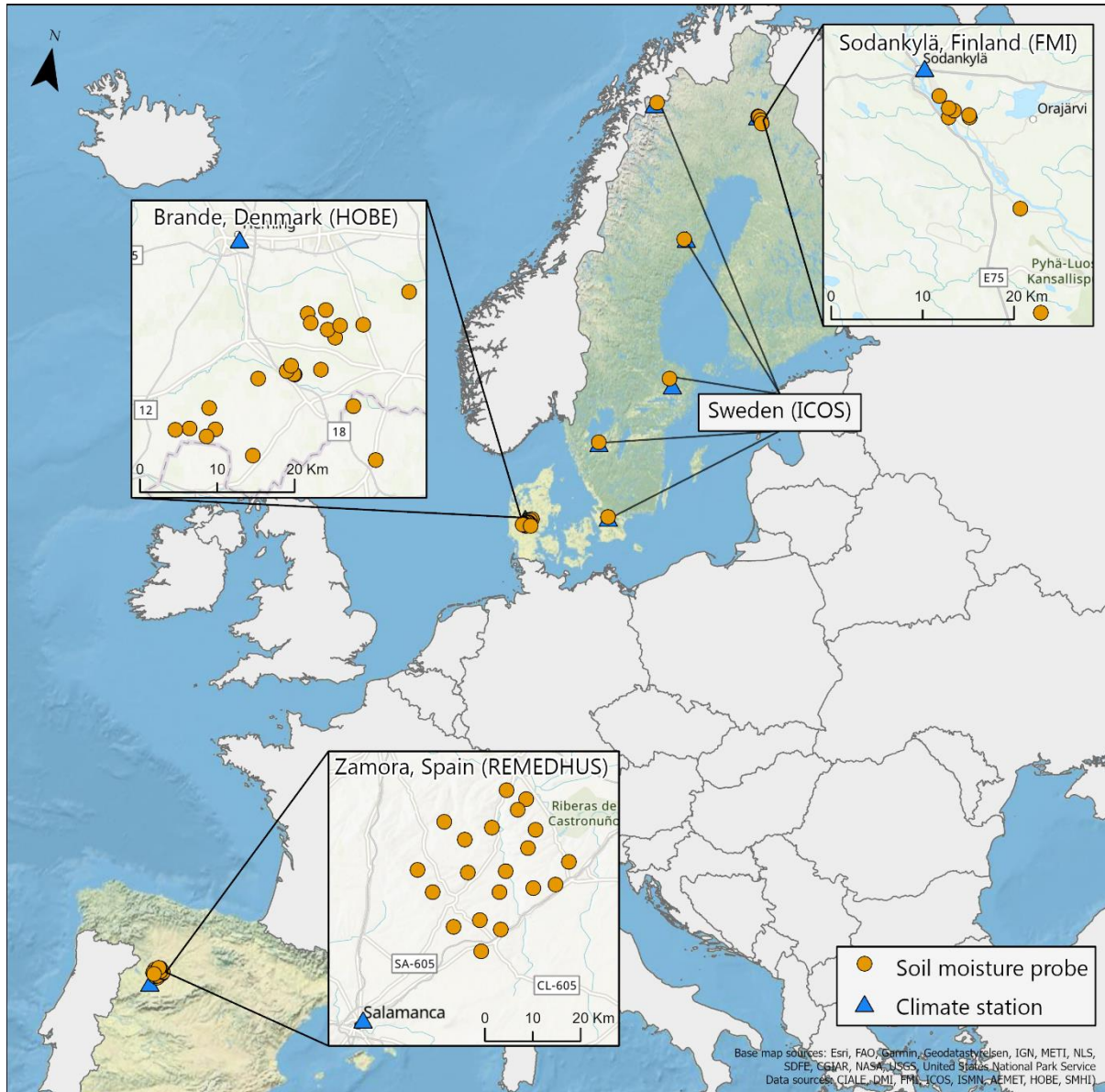


Figure 1. Geographical locations of the study sites in Europe with soil moisture (SM) probes used for calibrating and validating the model. The location of the SM probes is marked by orange circles and the location of the climate probes associated with each study area is marked by blue triangles.

3.1.2. Topography

The topographic profiles of the probes are distributed primarily in three clusters (Fig. 2) at low elevation-low slope, high elevation-low slope, and high elevation-high slope. The HOBE probes have a narrow distribution in elevation of less than 100 m but exhibit some outliers in slope with the largest overall spread across all networks at 18.5%. Most ICOS and FMI probes follow a similar pattern as the HOBE probes, with gentle slopes (<5%) at low elevations (<200 m.a.s.l). The REMEDIHUS probes are situated at higher elevations in the range 650-900 m.a.s.l with slopes in two distinct clusters of 1-5% and 9-15%.

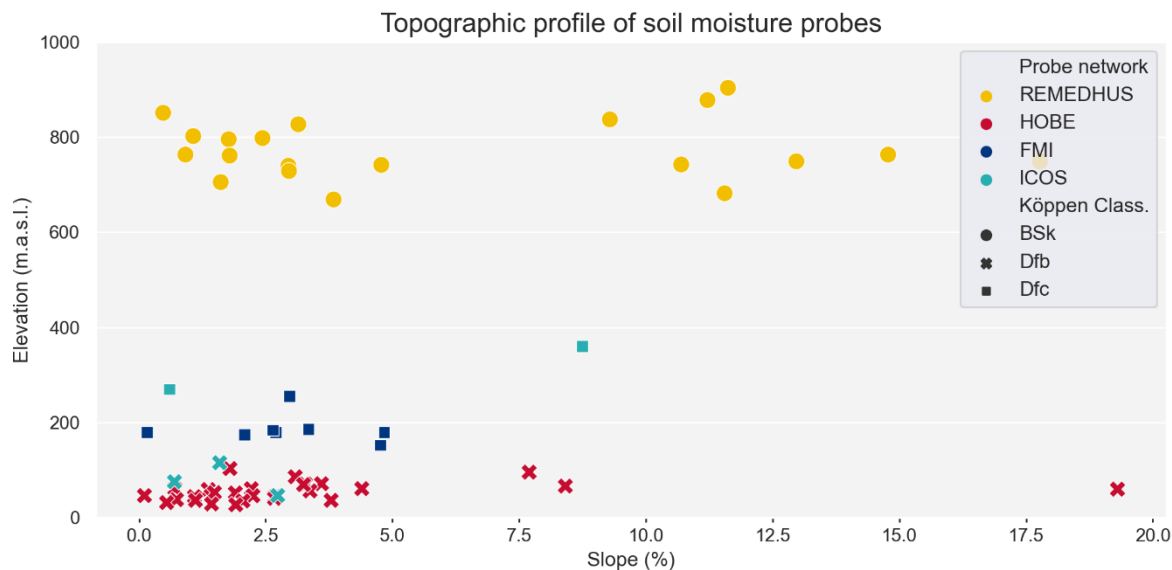


Figure 2. The topographic profile (slope and elevation) of each soil moisture probe used in the model. Probe networks are differentiated by color and the Köppen climate classification is marked by a symbol, where BSk (cold semi-arid) is a filled circle, Dfb (warm-summer humid continental) is an x, and Dfc (subarctic) is a square.

3.1.3. Land cover

The dominating land cover type as classified by CLC (European Environmental Agency 2018) in the dataset (Fig. 3) is *non-irrigated arable land* (45.4%) followed by *coniferous forests* (21.3%), which combined constitute 66.7% of all samples. The remaining land cover types are different types of *agricultural land covers*, *herbaceous and shrub types*, *sand*, and *peat bogs*. The HOBE and REMEDHUS probes account for 38.1% and 40.1% of all samples in the dataset, respectively. The probes in these two networks are primarily located on various *agricultural land covers*, *coniferous forest*, and to a lesser extent, *sand*, and *smaller herbaceous land covers*. The FMI and ICOS probes make up the remaining samples in the dataset at 12.9% and 8.9%, respectively. Due to the subarctic climate types of the FMI and some of the ICOS probes, their primary land cover type is *coniferous forest* and *peat bogs*.

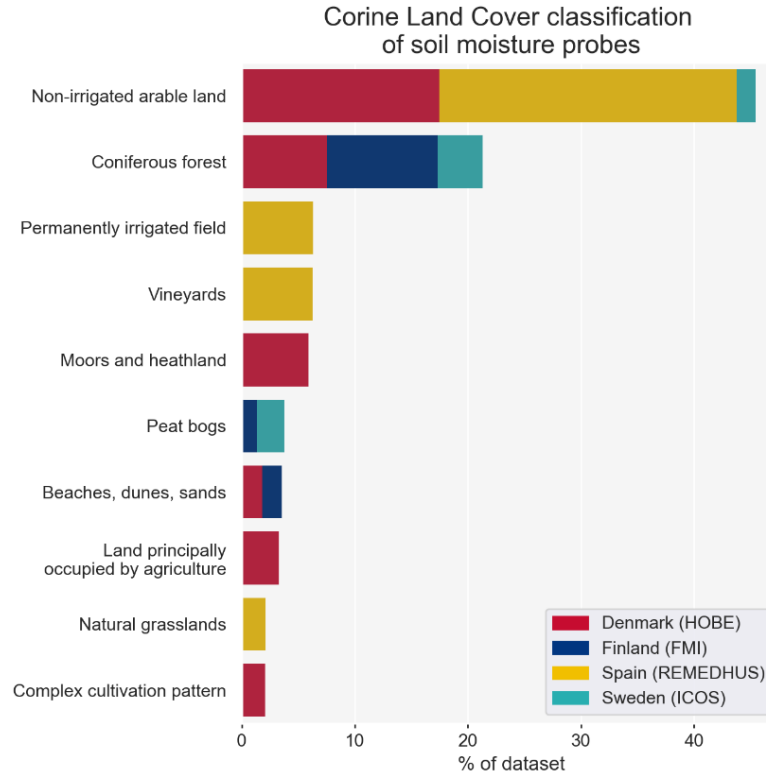


Figure 3. Distribution of land cover class (vertical) as classified by the Corine Land Cover 2018 (CLC 2018) classification by region (horizontal). Values are presented as cumulative percentages of the entire dataset used in the model after outliers, snow-covered periods, and false readings have been removed.

3.2. Data

The data used, the pipeline for converting the various types of data to a homogenous dataset, and the deep learning model (DLM) are hosted on <https://github.com/nicklts/RNN-SM-Model>. The original data was acquired from multiple sources listed in Appendix A.

3.2.1. In situ measurements of soil moisture and soil temperature

The SM probe data was retrieved from the ISMN (Dorigo et al. 2011; Dorigo et al. 2013) (HOBE, FMI, and REMEDHUS) and ICOS in volumetric units (m^3/m^3). For networks from ISMN, each probe provides hourly measurements of volumetric SM ($\pm 0.02\text{-}0.05 \text{ m}^3/\text{m}^3$ (Delta-T Devices Ltd 1998; Visconti et al. 2014; Bellingham 2015; Caldwell et al. 2018)) and soil temperature (TS) ($\pm 0.6 \text{ }^\circ\text{C}$ (Bellingham 2015; Campbell Scientific 2021)) in addition to information about the soil texture. Soil textures were measured in situ for 26 of the HOBE probes while the last two from the HOBE network and all other probes were inferred from the Harmonized World Soil Database v1.2 (HWSD) (Fischer et al. 2008). The soil texture is described as clay, silt, and sand fractions, amount of organic carbon, and base saturation. The ICOS probes sample both SM and TS at half-hour intervals. Both data sources have been resampled to daily mean SM and daily maximum TS (TS_{max}) and only the measurements at 0-0.05 m depth are used from each probe network. The ICOS network consist of several study sites, each site containing up to four sub-probes within 10m^2 . A mean SM value between these sub-probes have been used for each study site. The TS_{max} was used to filter sample points with frozen soil, where values $\leq 0.0^\circ\text{C}$ were removed from the dataset. The subsequent spatial datasets were integrated with the point-based in situ measurements by extracting the value of

the cell at the spatial locations of the SM probes using the coordinates provided in the metadata of each SM probe.

3.2.2. Sentinel-1 data

The Sentinel-1 SAR images were acquired as Level-1 Ground Range Detected (GRD) Interferometric Wide Swath medium resolution (10 m ground sampling distance (GSD)) images from both ascending and descending orbits. As preprocessing steps performed prior to acquisition, these images were detected, multi-looked, and projected to ground range using an Earth ellipsoid model (Piantanida et al. 2019). Further preprocessing of the SAR products after acquisition was required before using the images in the model. This preprocessing workflow is described by Filipponi (2019) and involves steps to radiometrically and topographically correct the images (Fig. 4) using the Sentinel Application Platform (SNAP) v7.0 (European Space Agency 2019) application.

The first step after sub-setting the study area was applying an external orbit file that specifies the exact orbit position of the satellite at the time of recording, as the information included in the metadata is often inaccurate.

Next, different types of noise were removed from the image by first normalizing backscatter values across the entire scene to reduce discontinuities between sub-swaths. The border along each scene has noise artifacts caused by preprocessing from the raw Level-0 data to Level-1 (Ali et al. 2018). These artifacts are removed to ensure consistent readings throughout the time-series. At this step, the polarizations were also chosen, which for Sentinel-1 GRD images is either VV or VH. For this study, only the VV polarization is used due to the limited potential of VH as a consequence of its sensitivity to volume scattering (Karjalainen et al. 2004; Patel et al. 2006; Gao et al. 2017) The radiometric calibration converts the magnitude of pixels to Sigma Nought (σ^0):

$$\sigma^0 = \frac{DN^2}{A_\sigma^2} \quad (1)$$

where DN is the pixel amplitude and A_σ is the look-up table (LUT) conversion value for σ^0 provided in the product annotations (Miranda and Meadows 2015). The Sigma specifies the strength of reflection in terms of the geometric cross section of a conducting sphere, and represents the radar cross section of a distributed target over that expected from an area of one square meter (Filipponi 2019).

After calibrating the image it was passed through speckle filter using the Lee Sigma operator (Jong-Sen Lee et al. 2009), which reduces the noise of individual pixels by filtering in a 7x7 window across the image. This process eliminates many of the false variations observed in the image due to shifting soil geometry, vegetation texture, and other sporadic obstructions, at the expense of a loss in detail for individual pixels. The output is given as σ^0 in linear units, which

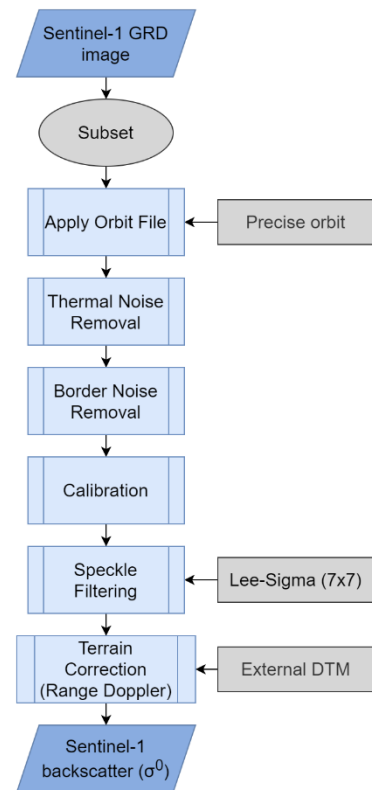


Figure 4. Sentinel-1 SNAP (ESA 2019) processing workflow for ground range detected (GRD) images.

is a normalized dimensionless number expressing the backscattering coefficient perceived by the SAR from a surface.

The slope of the sensed surface leads to distortions due to the side-looking geometry of the SAR. Terrain corrections compensate for these distortions to produce closer real-world representations. The Range-Doppler orthorectification method (Small and Schubert 2008) uses the orbit state vector information, the radar timing annotations, and the slant ground range conversion parameters provided in the metadata of each scene along with the Digital Terrain Model (DTM) (Table 2) to derive the precise geolocation.

The outliers are typically classified as being several orders of magnitude higher in pixel value than the median value of the image. The outliers in the VV polarization are often due to backscatter from corner reflectors, such as buildings, and appear as bright dots in the image (Fig. 5). Objects similar in physical size to the width of the wavelength may also result in strong backscattering. These outliers are non-beneficial for the estimation of SSM and have therefore been removed from the data. Outliers were determined using a z-score threshold of ± 2 after a manual investigation of different scores to find the lowest threshold before affecting non-outliers. After filtering outliers, the maximum σ^0 value in the dataset was 0.35.

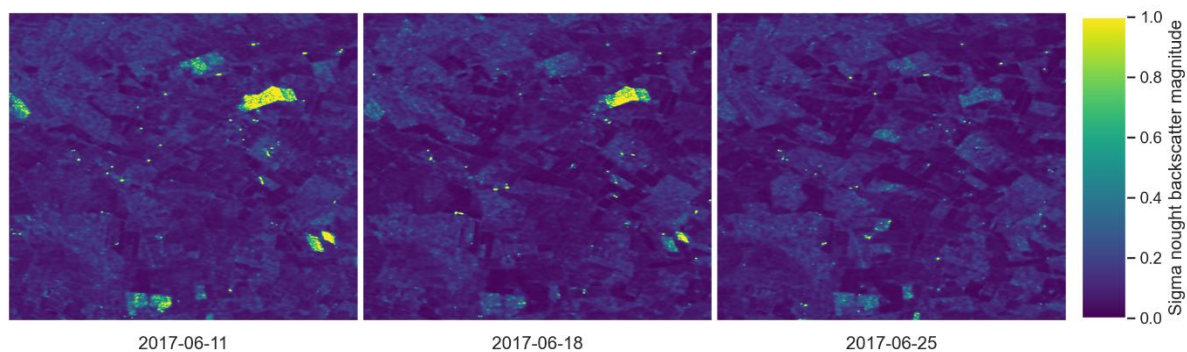


Figure 5. Sentinel-1 SAR images over a 9 by 5 km section of the HOBE study area. Sigma nought (σ^0) values above 1 for illustration purposes. Outliers are presented as bright yellow dots or yellow fields where the soil has been tilled.

3.2.3. Sentinel-2 data

The Sentinel-2 images were retrieved either as fully preprocessed Level-2A or partially preprocessed Level-1C requiring further corrections. The Level-1C images are orthorectified using a Digital Elevation Model (DEM) to project it in cartographic coordinates. Per-pixel radiometric measurements are provided at Top Of Atmosphere (TOA) and resampled to 10, 20, and 60 m GSD depending on the native resolution of the different spectral bands (European Space Agency 2015). The Level-1C images are processed to Level-2A using the Sen2Cor processor (Main-Knorn et al. 2017), which involves a series of steps for atmospheric correction and reflectance conversion (Fig. 6).

The first step in the process is the extraction of a scene classification, which produces a probability map of snow and cloud cover including a classification map (Richter et al. 2011). The scene classification is used to correct for cirrus clouds in the Level-1C image. Next, the aerosol optical thickness (AOT) is derived from the Dense Dark Vegetation (DDV) algorithm (Kaufman and Sendra 1988) based on the correlation between the reflectance in short-wave infrared (band 12) and visible spectrum (bands 4 and band 2) (Richter et al. 2011). The look

up table, which in the Sen2Cor processor refers to libRadtran4 (Mayer and Kylling 2005) provides parameters for different aerosol types depending on geographical location and seasonality. The water vapour retrieval over land is calculated with the Atmospheric Pre-corrected Differential Absorption algorithm (Schläpfer et al. 1998; Main-Knorn et al. 2017), which uses the bands B8a and B9 for reference in an atmospheric window region and measurement in the absorption region, respectively. The final step in the process is the conversion of TOA to bottom of atmosphere (BOA) reflectance using the derived atmospheric maps, which produces the Level-2A atmospherically corrected BOA image. Additionally, the output from the Sen2Cor processor includes a scene classification but for the purpose of this study has been limited to the cloud and snow probability masks.

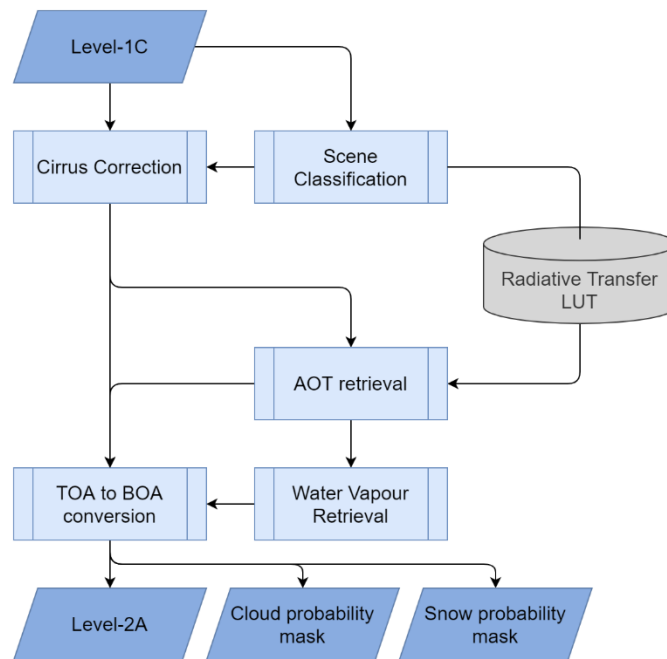


Figure 6. Sentinel-2 Sen2Cor (Richter et al. 2011; Main-Knorn et al. 2017) processing workflow for converting Level-1C images to Level-2A. The Radiative Transfer look-up table (LUT) refers to an external database.

The Level-2A images are further processed to derive an NDVI (Eq. 2) and Normalized Difference (Vegetation) Water Index (NDWI) (Gao 1996) (Eq. 3) profiles for each scene. The NDVI uses the normalized difference between the near-infrared band (B8a) and the red band (B4) to produce a measure of the amount of healthy vegetation. The NDWI uses the normalized difference between the short-wave infrared band (B12) and the near-infrared band (B8a) to create an index of water content in the leaves:

$$NDVI = \frac{NIR - VIS_{red}}{NIR + VIS_{red}} \quad (2)$$

$$NDWI = \frac{NIR - SWIR}{NIR + SWIR} \quad (3)$$

These two scene VIs have a GSD of 10 m after resampling the short-wave infrared band from 20 m to 10 m. For each scene, clouds and snow has been filtered out at a 90% threshold using the probability maps created from the scene classification in the Sen2Cor processor. A time-series Vegetation Index (VI) profile was created for each SM probe by interpolating between

each known point with a linear function. The interpolation is limited to 30 days before and after each known point to limit the error from the assumption of constant linear change over time.

3.2.4. Meteorological data

The climate data includes hourly or daily measurements of air temperature (TA) and precipitation at weather stations in or near the study areas (<45 km mean distance) (Fig. 1). All readings were resampled to daily measurements, from which a minimum (TA_{min}), mean (TA_{mean}), and maximum (TA_{max}) temperature were calculated in addition to cumulative precipitation. The number of cumulative days with precipitation of <0.1 mm was added as a variable.

3.2.5. Topographic and land cover data

Topographic information about each study area has been derived from local DTMs (Table 2), where vegetation and artificial structures have been removed. From these the elevation, slope, and aspect of each SM probe have been calculated. The aspect has been split into a vector with an x (Eq. 4) and a y (Eq. 5) component for better model interpretation:

$$Aspect_x = \cos(Aspect_{degrees}) * \frac{\pi}{180} \quad (4)$$

$$Aspect_y = \sin(Aspect_{degrees}) * \frac{\pi}{180} \quad (5)$$

The land cover type was read from the CORINE Land Cover 2018 (CLC) classification (European Environmental Agency 2018), which has been produced primarily with Sentinel-2 images and gap-filled with Landsat-8 images (Büttner et al. 2017). The spatial resolution of CLC is 100 m with a minimum mapping unit of 25 ha and width of 100 m.

Table 2. Specifications for the digital terrain models (DTM) used for calculating topographic indices.

Source name	Region	Network	Producer	Spatial resolution	Horizontal / Vertical accuracy
DHM-2007/Terræn	Denmark	HOBE	Styrelsen for Dataforsyning og Effektivisering (2007)	1.6 m	0.05 m / 0.15 m
Elevation model 2 m	Finland	FMI	National Land Survey of Finland (2021)	2 m	0.3 m / 0.3 m
MDT05	Spain	REMEDHUS	Centro Nacional de Información (Geográfica 2021)	5 m	- / -
GSD-Höjddata, grid 2+	Sweden	ICOS	Läntmateriet (2020)	2 m	- / -

3.2.6. Evaluation of intervariable relationships

An analysis of the variables used in the model is crucial prior to training the network. This will either highlight important variables, which are likely to contribute significantly to the learning ability of the network or identify redundant variables. Any variable without significant contribution will impede the network in learning the correct statistical relationships.

Intervariable relationships were assessed using statistical measures and qualitative analysis. Correlations were calculated using the Spearman's rank correlation coefficient due to the non-parametric nature of the data. Variable distributions were qualitatively assessed using violin plots rather than boxplots because the former includes a kernel density estimation of the underlying distribution. This makes it possible to discern whether the data is multimodal and where the concentration of values are, as reflected by the amplitude of the density distribution. Density distributions, or feature occurrences, were evaluated using heatmaps to find values with large agreements and non-linear relationships.

3.3. Deep learning model

3.3.1. Model architecture

The processing of input variables to a homogenized tensor ready for model ingestion is set up in a pipeline structure written in Python 3. The pipeline takes any of the given variables, processes them, and maps them to the correct date for each SM probe. Input variables in the model may be classified as either static or dynamic, where the latter is always temporal but either may be point-based or spatial (Fig. 7). These variables are combined into a spatio-temporal dataset, containing a time-series of all variables associated with each probe. For spatial data, the pixel value at the location of the probe is used as the associated value. The time-series datasets are stacked into a 3-dimensional tensor corresponding to batch size (number of probes), timesteps (length of time-series), and features (number of variables). The dataset contains variables at different scales and is therefore normalized. The datasets are ingested into the DLM along with the measured soil moisture, which is used to calibrate and finally validate the predictions.

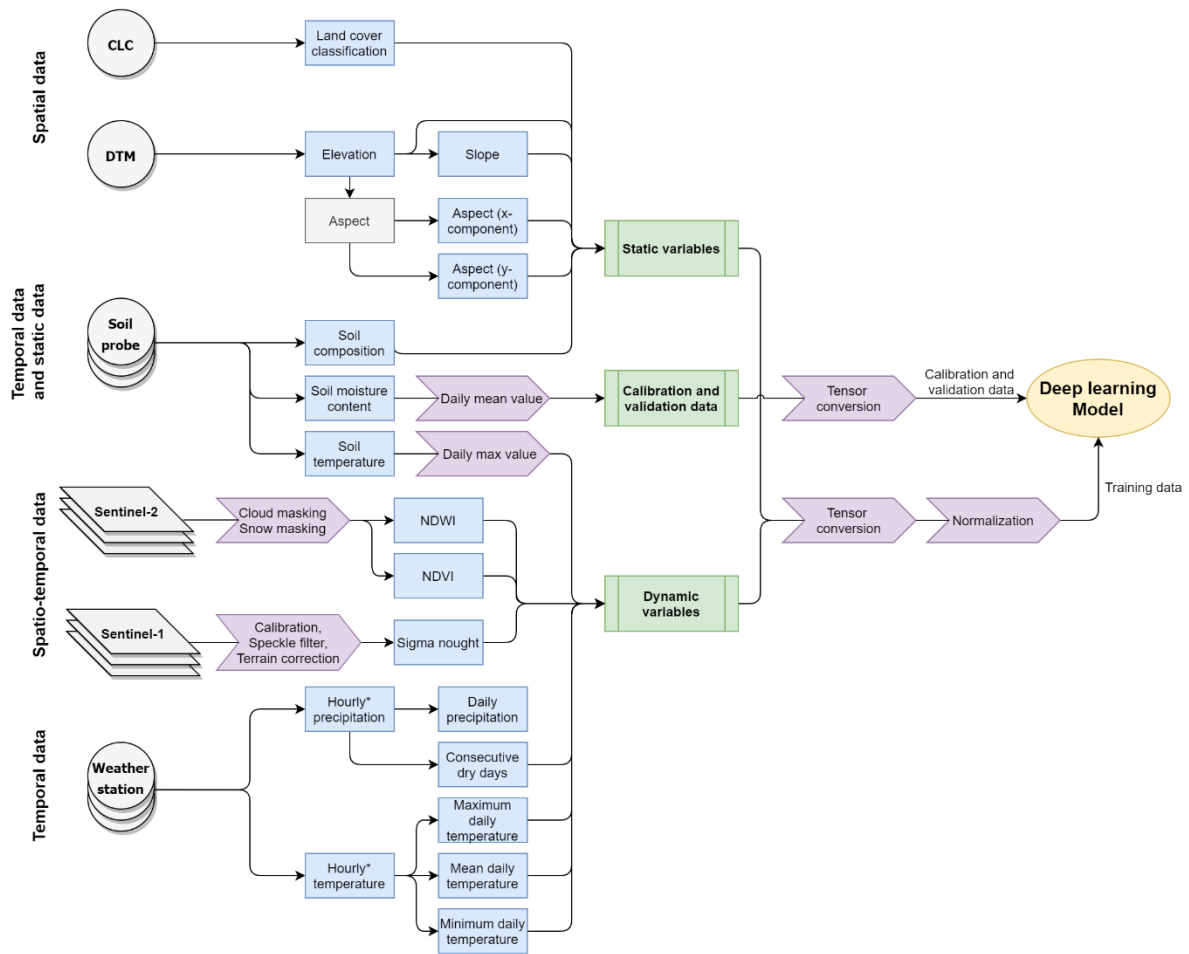


Figure 7. Simplified deep learning model workflow with multiple input types. Variables denoted by asterisks (*) are in most cases obtained as hourly data but are for some weather stations given as daily sum, mean, min, and max.

The DLM has been trained on three variations of the full dataset independently to evaluate the importance of some variables and to test the limitations. The first variation uses all SM probes and all variables and will henceforth be referred to as the DLM_{full} . The second variation also uses every SM probe but is limited to only including the dynamic variables and land cover and hence is named the $DLM_{minimum}$. The last variation uses only SM probes located on either *non-irrigated arable land* or permanently irrigated field land covers and is also limited to only dynamic variables. This model is a specialization of agricultural SM prediction and hence is named the $DLM_{agriculture}$.

The DLM uses a leave-one-out approach to calculate the accuracy of the predictions for each SM probe (Fig. 8). This approach involves omitting a single SM probe from each batch, while training and validating the predictions on the rest. The data ingested into the model is split in an 80/20 percent division along the batch length, which results in 48 probe time-series for training and 12 for validation. The probes used for validation are randomized between each iteration of the model to reduce interpreter and model bias. The model is reset between each batch to ensure that no information about the test set is carried over into the training and validation set. Each batch consists of a number of mini-batches equal to the number of probes in the training set. This means that for each mini-batch, the entire time-series for one probe is ingested into the model and no information from the previous time-series dataset spills over.

Data gaps arising from sampling methods longer than one day, such as Sentinel-1 and Sentinel-2 data, or longer continuous gaps in the SM data lead to incomplete time-series. Inconsistent dataset lengths are incompatible with the model architecture and thus each dataset has been padded to fit the maximum time-series length of 883 days. The padding type is a resampling of the dataset to consistent 1-day timesteps.

The model was trained for 20 epochs, which was determined through a randomized grid search for hyperparameters to be the optimal length before overfitting. Each model run was repeated ten times for each test probe to diminish the effects of ‘bad’ weights in the initialization of the network and unrepresentative validation probes. A total of 41442 samples across 61 probes were used for training, validation, and testing the model. The model architecture is built on two sequential Long-Short Term Memory (LSTM) layers. Various other model architectures were assessed, including SimpleRNN, Gated Recurrent Units (GRU) (Cho et al. 2014), 1-dimensional convolutions, and regular NN layers. However, none of these achieved the same accuracy as the LSTM and stacking two or more architecture types resulted in overfitting and thus poor test accuracy. The relatively small sample size and complexity of variable relationships were limiting factors in these results as more units or hidden layers resulted in overfitting. The highest accuracy was achieved by stacking two LSTM layers, each containing 16 units, and training for 20 epochs with a batch size of one.

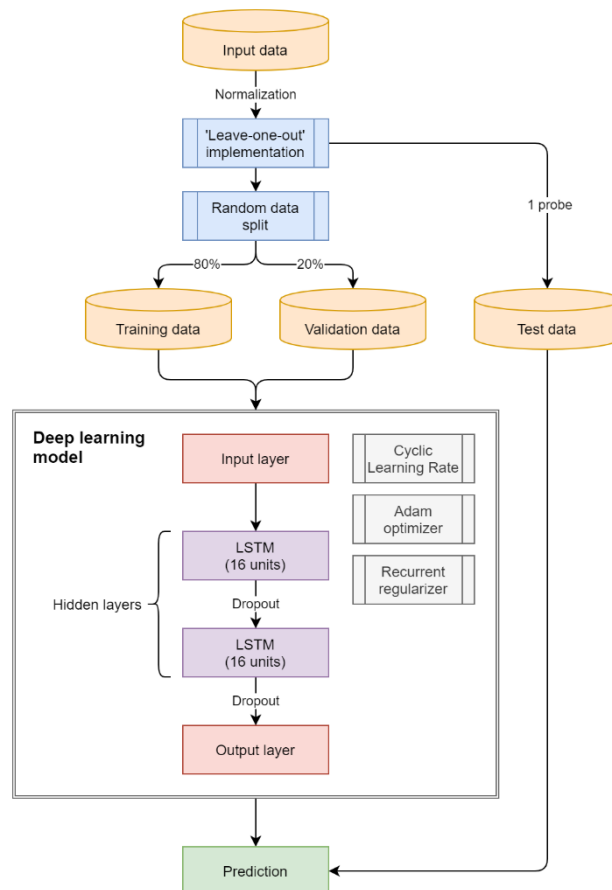


Figure 8. Deep learning model and recurrent neural network (RNN) architecture.

3.3.2. Model hyperparameters

The DLM is built as a sequence-to-sequence RNN on the Tensorflow platform (Google 2020) and assembled using the high-level Keras (Chollet 2020) library. The network consists of an input layer, two LSTM cells (Hochreiter and Schmidhuber 1997) with 16 units in each, and an output layer. The input layer simply specifies which dimensions are being used by the training data, while the output layer changes the dimensions of the output from the LSTM cells. The key to the LSTM is the cell state C (Fig. 9) which allows information to move through the layers unchanged (Géron 2019) and gives the cell its long-term memory capacity. Each LSTM cell consists of multiple memory gates that dictate which information and to what extent is included in the cell state. The first gate in this is the forget gate f_t (Gers et al. 2000), which decides what information is kept in the cell state by:

$$f_t = \sigma(W_f * [h_{t-1}, x_t] + b_f) \quad (6)$$

where σ is a sigmoid function squashing the output to a range of 0 to 1, h is the hidden state, x is the input data, and W and b are the weight matrices and the bias vector parameter, respectively, which are learned during training. The subscript t indexes the time step and the subscript f denotes the gate.

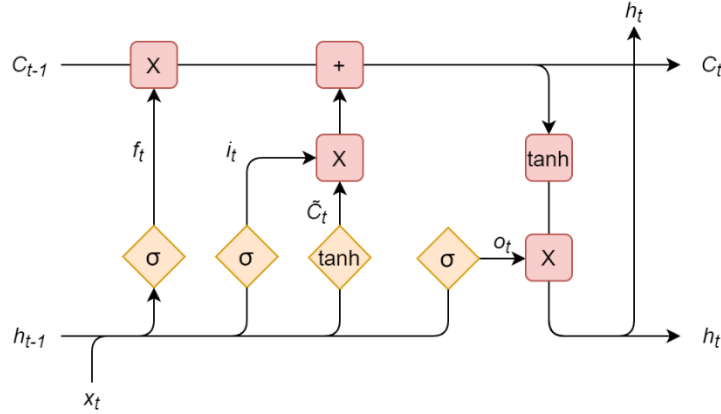


Figure 9. Long Short-Term Memory (LSTM) cell (Hochreiter and Schmidhuber 1997; Gers et al. 2000) with layers (yellow diamonds) and pointwise operations (red squares).

The second gate is the input layer gate i_t and decides which values will be updated using the function Eq. 7. A new candidate value \tilde{C}_t is created by the tanh function and combined with i_t by point-wise multiplication to create an update to the state. The tanh function differs from the sigmoid functions from the previous layers as it scales the values between -1 and 1 to avoid exploding gradients:

$$i_t = \sigma(W_i * [h_{t-1}, x_t] + b_i) \quad (7)$$

$$\tilde{C}_t = \tanh(W_c * [h_{t-1}, x_t] + b_c) \quad (8)$$

Next, the cell state C_t is updated from the prior state C_{t-1} using the output from both the forget gate and the input gate:

$$C_t = f_t * C_{t-1} + i_t * \tilde{C}_t \quad (9)$$

The cell state is passed to the next hidden layer in the network, where the same process is repeated. The last gate is the output gate o_t which is responsible for the output h_t of the LSTM. The input values are first passed through a sigmoid function and then combined with cell state, which has been passed through a tanh function:

$$o_t = \sigma(W_o * [h_{t-1}, x_t] + b_o) \quad (10)$$

$$h_t = o_t * \tanh(C_t) \quad (11)$$

The hidden state h_t is duplicated to act both as an output for the layer and as an input to the next cell. The cell state C_t is passed to the next cell either modified by the input gate or unchanged. Once the input values have been through the LSTM cell, they are passed through the output layer (Fig. 8), which consists of a regular perceptron layer (Rosenblatt 1958) with a single unit. This step is meant to reduce the dimensions of the output from the LSTM cell caused by the sequence-to-sequence prediction into a vector of identical size to the validation target:

$$Y = X * W \quad (12)$$

where Y is the output, X represents the matrix of input features, and W contains the connection weights.

The LSTM layers in the network are followed by a dropout layer, which randomly sets an input value to 0 at a rate of 10% per step during training. This teaches the network to be less dependent on any one neuron and thereby helps reduce overfitting when certain neurons become specialized during training. The second regularizer used in the network is a ridge regression (Hoerl and Kennard 1970), which adds a penalty term to the loss function during training to diffuse the weights:

$$L_{ridge}(\hat{\beta}) = \sum_{i=1}^n (y_i - x_i' \hat{\beta})^2 + \lambda \sum_{j=1}^p \hat{\beta}_j^2 \quad (13)$$

where $L_{ridge}(\hat{\beta})$ are the estimations of the true parameters, $\hat{\beta}$. y and x are the dependent and independent predictor variables, respectively, and λ is the regularization penalty, which is set to $1.0 * 10^{-4}$. The ridge regression is implemented on the recurrent connections on each LSTM unit.

The network implements the Adaptive Moment Estimation (Adam) (Kingma and Ba 2015) stochastic gradient descent method as the optimizer. The goal of the gradient descent method is to find the global minima in the loss function space, while avoiding local minima where the gradient descent may get 'stuck'. This is implemented mathematically by minimizing the objective function $J(\theta)$ parameterized by the model's parameters $\theta \in \mathbb{R}^d$ by updating the parameters in the opposite direction of the gradient g of the objective function $\nabla_{\theta} J(\theta)$ (Ruder 2016). Gradient descent is controlled by the learning rate η , which determines the size of the steps used to reach the minima. The stochastic gradient descent performs a parameter update for each training sample x_i and label y_i rather than the entire training dataset, which reduces training time but also leads to heavy fluctuations in the objective function:

$$\theta = \theta - \eta * \nabla_{\theta} J(\theta; x_i; y_i) \quad (14)$$

Adam reduces these fluctuations by computing adaptive learning rates for each parameter (Kingma and Ba 2015). It also stores an exponentially decaying average of past gradients m_t and past squared gradients v_t (Ruder 2016), which are the first moment (mean) and second moment (variance) of the gradients, respectively:

$$m_t = \beta_1 m_{t-1} + (1 - \beta_1) g_t \quad (15)$$

$$v_t = \beta_2 v_{t-1} + (1 - \beta_2) g_t^2 \quad (16)$$

m_t and v_t are initialized as vectors of 0's and become naturally biased towards zero (Kingma and Ba 2015), which is counteracted by computing the bias-corrected first and second moment estimates:

$$\hat{m}_t = \frac{m_t}{1 - \beta_1^t} \quad (17)$$

$$\hat{v}_t = \frac{v_t}{1 - \beta_2^t} \quad (18)$$

where parameters are set to 0.9 and 0.999 for β_1 and β_2 , respectively. The bias-corrected terms are used to update the parameters, which yields the Adam update rule:

$$\theta_{t+1} = \theta_t - \frac{\eta}{\sqrt{\hat{v}_t} + \epsilon} \hat{m}_t \quad (19)$$

where the parameter ϵ is set to $1.0 * 10^{-7}$.

The learning rate hyperparameter η is adjusted throughout the network training phase with a Cyclical Learning Rate (CLR) (Smith 2017) (Fig. 9). This allows the network to adapt the learning rate with respect to the loss function to find the minima more efficiently. The CLR is defined by a base learning rate set to $1.0 * 10^{-6}$, a max learning rate set to $2.0 * 10^{-3}$, and a step size of 250. The learning rate oscillates between the two learning rates during training, which helps prevent the gradient descent from becoming stuck in local minima, while also converging faster on a global minima (Smith 2017).

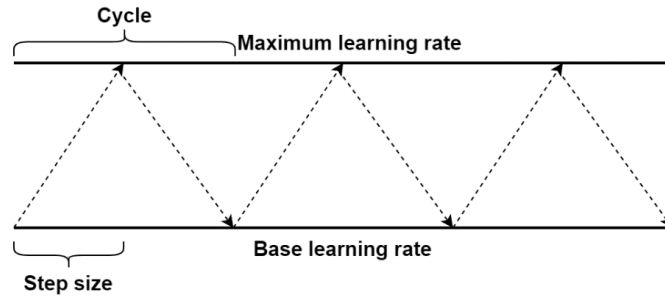


Figure 10. Illustration of the Cyclical Learning Rate (CLR) algorithm.

A summary of the DLM hyperparameters used for the model are presented in Table 3.

Table 3. Deep learning model (DLM) hyperparameters

Hyperparameter	Type	Description
Layer	LSTM	Depth: 2, units: 16
Regularizer (recurrent)	Ridge regression	Decay: $1.0 * 10^{-4}$
Dropout	Regular	Rate: 10%
Loss	Mean Absolute Error	
Optimizer	Adam	$\beta_1: 0.9, \beta_2: 0.999, \epsilon: 1.0 * 10^{-7}$
Callback	CLR	Base learning rate: $1.0 * 10^{-6}$, Max learning rate: $2.0 * 10^{-3}$ Step size: 250
Epochs		20
Batch size		1

3.3.3. Evaluation metrics

The loss function of the network and results were computed using a mean absolute error (MAE) of the entire sequence of each SM probe time-series:

$$MAE = \frac{\sum_{i=1}^n |y_i - x_i|}{n} \quad (15)$$

where y is the observed value and x is the measured value of SSM, n is the number of samples and subscript i denotes the respective sample of the sequence. MAE was chosen over the conventional Root Mean Square Error (RMSE) to weigh errors of equal proportion similarly. As volumetric SM reflects a scale of values ranging from 0-100% in equal intervals, adjusting the weights in the network by similarly equal losses is the most intuitive metric. For the evaluation of the statistical distributions of predictions, the absolute error between each predicted and observed value were calculated. The MAE for the validation results were 6.2-8.4% and varied due to the small heterogenous dataset.

3.3.4. Performance of model variations

The three model variations DLM_{full} , $DLM_{minimum}$, and $DLM_{agriculture}$ were evaluated on representative datasets, with all land covers for the former two and exclusively *permanently irrigated field* and *non-irrigated arable land* for the latter. Performance was measured as MAE for all samples in the dataset on both validation and test data. While the validation performance was inconclusive as to which model performed better, the test results implied a stronger connection between number of parameters and performance.

3.3.5. Evaluation against existing soil moisture products

The accuracy of the model was evaluated against the ECV_SM v5.2 combined product (Liu et al. 2011; Dorigo et al. 2015; Dorigo et al. 2017; Gruber et al. 2019) and CSM (Bauer-Marschallinger et al. 2019) products at ~25- and 1-kilometer resolution, respectively. The

ESV_SM is a merged product produced by a combination of active and passive sensor datasets (Gruber et al. 2019), hereunder the passive sensors SMOS (Kerr et al. 2001), AMSR2 (Imaoka et al. 2010), SMAP (Entekhabi et al. 2015), FY-3B, GPM, and active sensors ASCAT-A and ASCAT-B. All datasets are resampled to 0.25 arc-seconds using a Hamming-window approach and to daily timestamps (00:00 UTC) using a nearest-neighbour search (Gruber et al. 2019). The CSM product is created from Sentinel-1 A and B active sensor backscatter by scaling azimuthally corrected radar backscatter measurements between the historically lowest and highest observed values (for each individual grid location) (Bauer-Marschallinger et al. 2019). The bottom 10% and top 10% of perceived backscatter values from the Sentinel-1 data has been removed prior to this scaling to reduce effects from outliers. The CSV product relies on the same Sentinel-1 images as the model and hence results would be more comparable than ECV_SM, where there may be up to a 24-hour difference in sampling time.

The ECV_SM and CSM products are produced as datasets of different spatial resolution and must be reduced to point-based measurements for evaluation. The same method for extracting pixel values from the spatial dataset in the model was used here to convert gridded data to point-based measurements. Each grid, or pixel, encompassing the position of the respective SM probe was read and stored with the date of measurement. These were then merged with the predictions by the DLM to produce a table of observed and predicted values (Appendix B). For dense probe networks this resulted in a duplication of pixel values from the ECV_SM product for multiple SM probes. Additionally, the ECV_SM is an iterative product, which is validated on in situ probes between versions, hereunder the REMEDHUS probes. This will likely lead to better performance by this product on these probes.

4. Results

4.1. Statistical relationships of model variables

4.1.1. Linear correlations

The linear correlations r of the variable sets were assessed (Fig. 11 & 12) to determine if any variable was likely to have a significant impact on the results of the model. The land cover and aspect variables were not included in this assessment due to their nominal and non-centered distribution, respectively. Static and dynamic variables have been separated as static values are repeated for every sample point in the time-series. For the static variables (Fig. 11), the highest independent linear correlations are found between the clay, silt, and sand fractions and elevation with r between 0.7 and 0.9. This negative relationship shows a decrease in grain size with higher elevations, signified by a higher concentration of clay and silt. Base saturation and slope have the lowest correlations ($r \leq 0.2$) among all the variables.

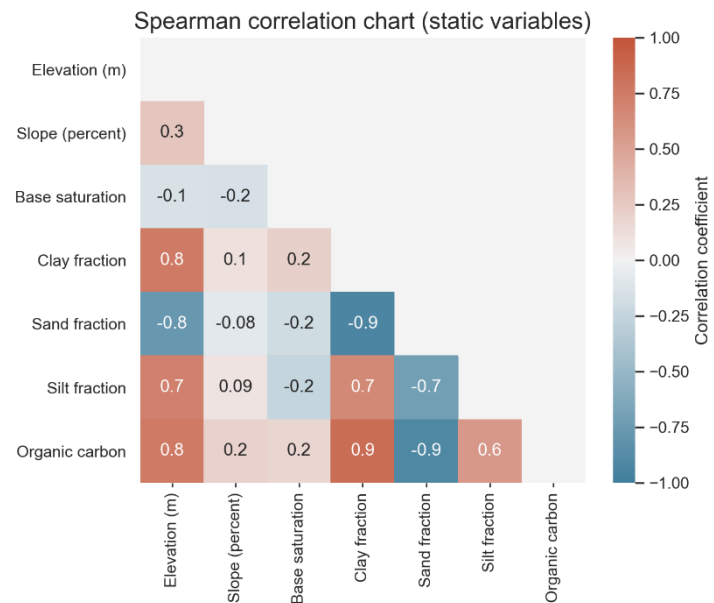


Figure 11. Spearman correlation coefficient matrix for static variables. Coefficient ranges from -1 (negative relationship) through 0 (no relationship) to 1 (positive relationship).

For the dynamic variables (Fig. 12), the highest independent linear correlations are found between TA and TS_{max} with $r = 0.9$, indicating a strong positive relationship between these variables. The TA show higher linear correlations with consecutive dry days than precipitation. This relationship is strongest for the TS_{max} and TA_{max} . The measured SSM is most strongly correlated with the temperature variables and of these the measured TS_{max} . Additionally, measured SSM has a weak correlation with σ^0 and precipitation at 0.2 and 0.08 and illustrates that these variables do not correlate linearly.

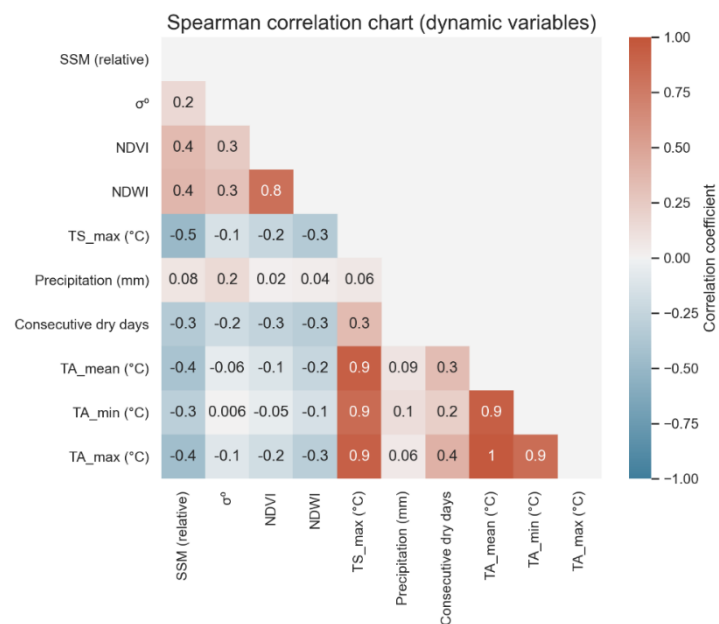


Figure 12. Spearman correlation coefficient matrix for dynamic variables. Coefficient ranges from -1 (negative relationship) through 0 (no relationship) to 1 (positive relationship).

4.1.2. Normalized distributions

The normalized distribution of the static variables (Fig. 13) reveals for soil texture and organic carbon the homogeneity of variables within study areas. Values are distributed in three large clusters corresponding to the larger study areas for Denmark, Finland, and Spain with some smaller distributions for the Swedish study areas. Base saturation is uniform across the study areas but does contain some outliers, giving the distribution a distinct positive tail. Elevation and slope represent the pattern in Fig. 2, with SM probes being at either high altitude for Spain or low altitudes for the rest. Similarly, the slope is centered around lower values for most SM probes but also contains some steep slope outliers in both Denmark and Spain. The mean aspect direction for the SM probes is approximately south but is distributed evenly in all directions except west.

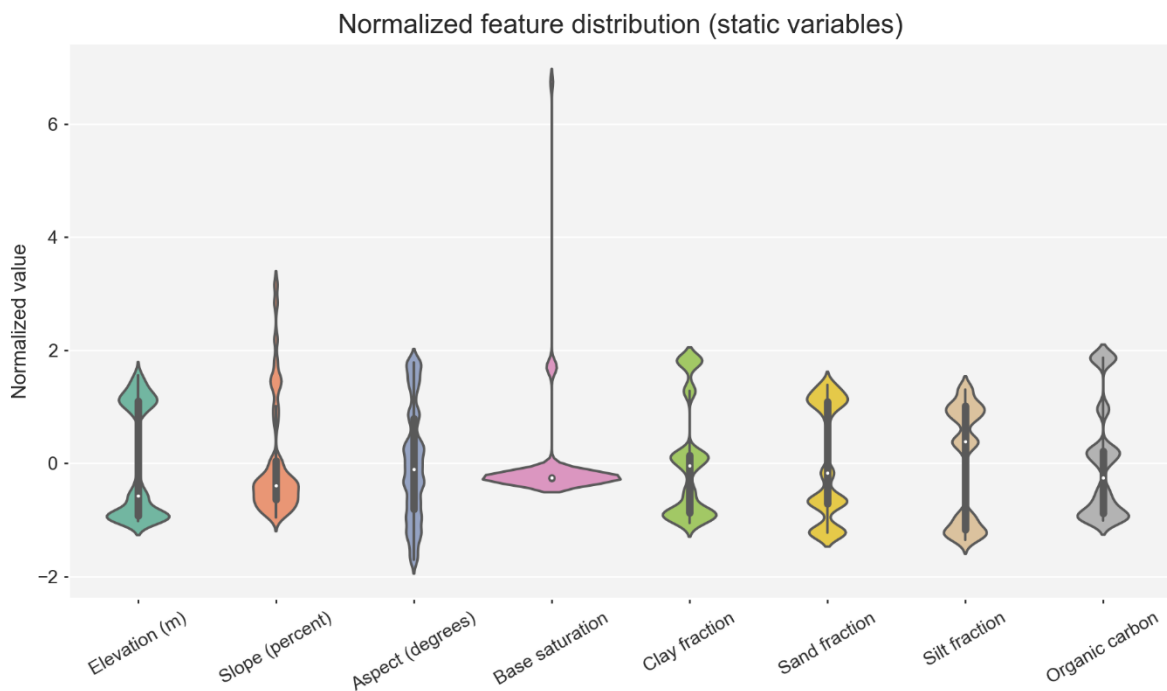


Figure 13. Normalized distribution of static variables with a mean μ of 0 and a standard deviation σ of 1.

The dynamic variables (Fig. 14) have a more normalized distribution less affected by outliers and clusters due to a more representative sample size. Values are mostly centered around the median with longer positive than negative tails. This is due to the limitation of how the variables are measured, such as SSM, where values may reach 0% or close to but will likely never reach 100%. Similarly, precipitation values are limited to zero but do not have a theoretical maximum, thus resulting in extremely long positive tails. However, TA show distributions in the opposite direction, where outliers are much lower than the observed median. This is likely also affected by the geographical distribution of sample points as fewer SM probes are in the high latitudes than the mid-to-low latitudes. TS_{max} does not have a similar distribution as TA and shows a longer distribution in the positive direction, likely caused by the exclusion of negative values.

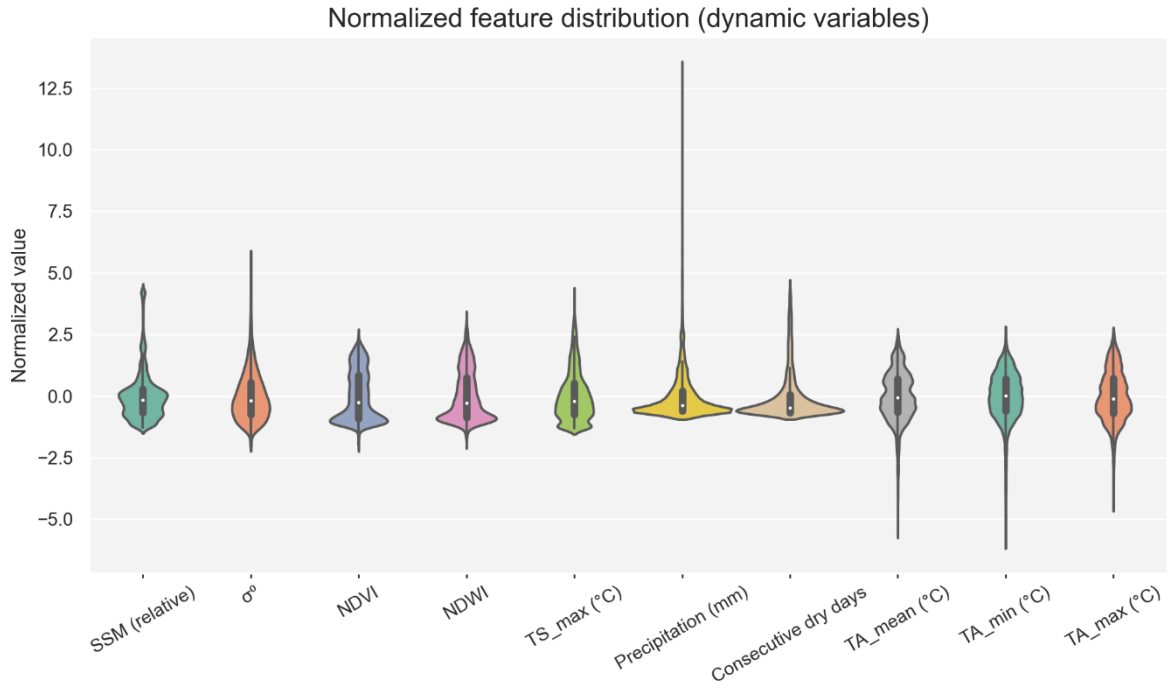


Figure 14. Normalized distribution of dynamic variables with a mean μ of 0 and a standard deviation σ of 1. The size of the violin plots is unscaled and not indicative of the sample size.

The normalized distribution of SSM across land cover types (Fig. 15) illustrate the heterogeneity of both median values and distributions. The median SSM occupy different niches for each land cover type, resulting in overlaps only during periods wetter or drier than the average. The exclusive agricultural land cover types, *non-irrigated arable land* and *permanently irrigated field*, have similar distributions despite the inherent difference in SM characteristics between the two types. The two land cover types, *permanently irrigated field* and *natural grassland*, which are exclusive to the REMEDHUS probes, show a similar distribution but with higher overall values for the latter. *Vineyards*, which are also exclusive to the REMEDHUS probes show a distinct pattern with very low overall values. Values for *peat bogs* are expectedly high overall but have a median centered relatively low due to the large number of observations at this range. The *coniferous forest* land cover has a median centered around 20% SSM but with a very elongated shape, especially in the positive direction. The range of measured SSM for *coniferous forest* exceed any other land cover types with values between 0-90%.

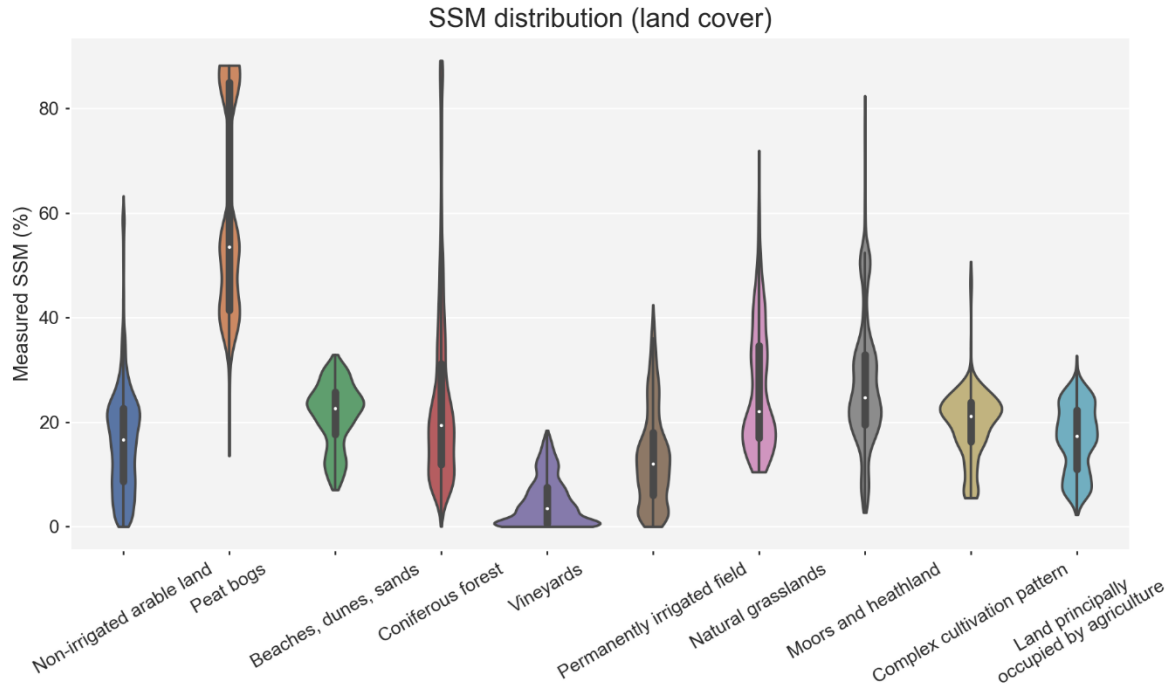


Figure 15. Distribution of measured surface soil moisture (SSM) for respective land cover types. The size of the violin plots is unscaled and not indicative of the sample size.

The regional distribution of SSM (Fig. 16) show the overall difference in SSM between regions for all land cover classes. Both Sweden and Finland suffer from a small sample size with just five and eight SM probes, respectively. Additionally, SSM distribution for Sweden has an undulating pattern caused by the heterogeneity of the SM probes. The bimodal pattern of Finland is likely a result of the land cover classes included in this region, which consists primarily of *coniferous forest* and to a lesser extent *peat bogs* and *sand*. The top-heavy concentration of high SSM values for Finland can be seen in the SSM distribution for *peat bogs* (Fig. 15), while the remaining two classes, *coniferous forest* and *sand*, roughly converge at 20% SSM. Spain has a strong unimodal distribution peaking just above zero, indicating an overall dryness across all SM probes in the network. The pyramid shape is a result of stacking various land covers with different median SSM values but a similar bias towards zero. The SSM values in Denmark have a semi-bimodal distribution with a pronounced peak and median at 20% SSM and a lesser peak at 10% SSM. This is largely a result of the geographical position in the mid-latitudes, an ample amount of precipitation, and including six of the ten land cover classes.

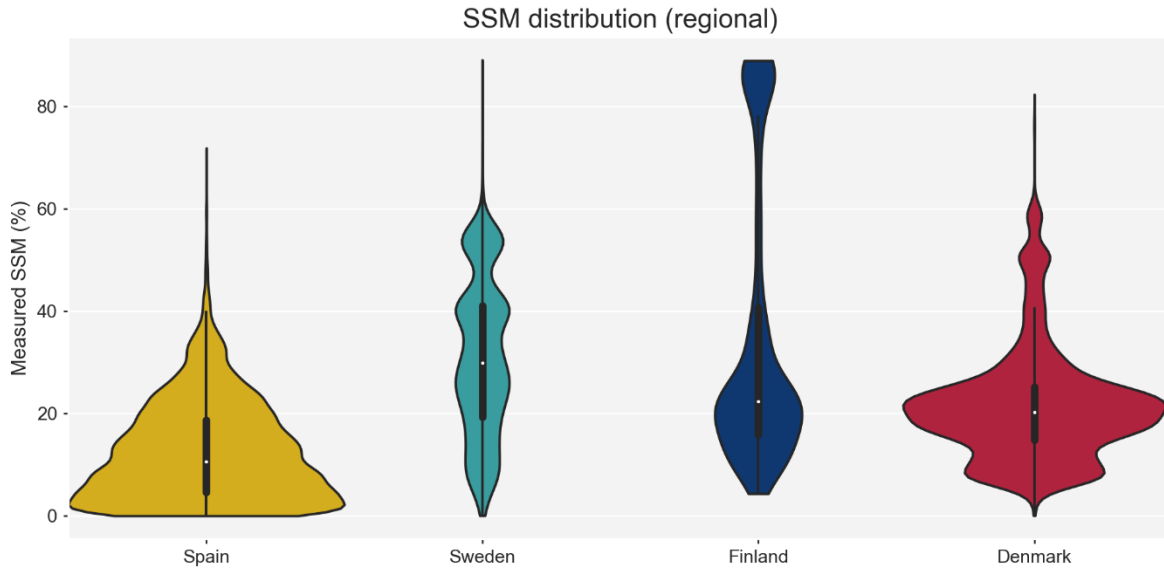


Figure 16. Distribution of measured surface soil moisture (SSM) for each region in the dataset. The size of the violin plots has been scaled according to the sample size of each region.

4.1.3. Sigma Nought backscatter and vegetation index feature distributions

As there is no empirical evidence in the data to support a linear correlation between SSM and σ^0 (Fig. 12), the physical response of the dielectric changes in the soil caused by moisture differences suggest a different type of relationship. Plotting the two variables in a heatmap (Fig. 17) shows a complex distribution of both variables. σ^0 values are measured mostly in the 0.02-0.20 range for all SSM values, while the latter has the most occurrences between 5-30%. While there is some indication of an overall negative relationship between the two variables, the highest magnitude of occurrences happens outside this relationship. The distribution of occurrences is not a result of aggregating multiple land cover classes and regions as the same relationship is observable across most SM probes. The distribution in σ^0 is therefore affected by additional parameters and variables besides SSM for both short- and long-term variations.

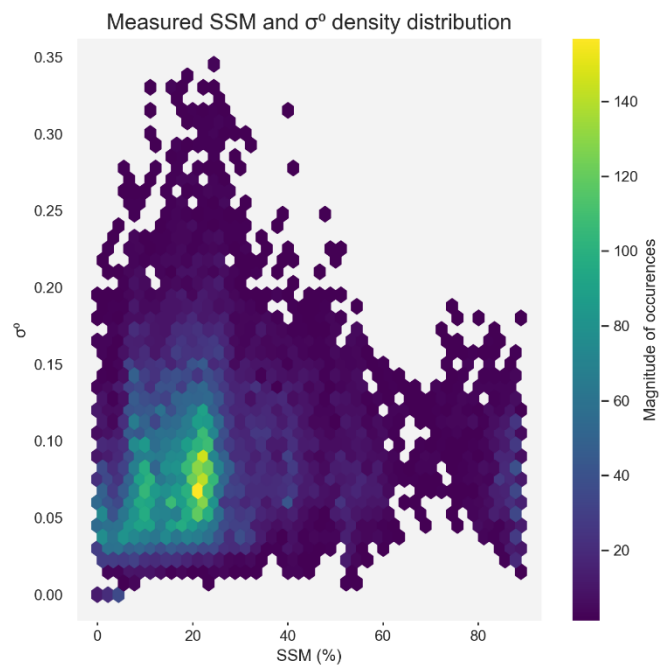


Figure 17. Density distribution of measured surface soil moisture (SSM) and Sigma Nought (σ^0). Each hexagon represents increments of 2.2% SSM between 0-89% and ~ 0.01 σ^0 between 0-0.35.

The direct relationship between σ^0 and land cover (Fig. 18) shows that for most land covers, the range of 0.02-0.20 established previously (Fig. 17) holds true. The two most represented, and hence most important land cover classes, *non-irrigated arable land* and *coniferous forest*, occupy different niches in the microwave spectrum. The *coniferous forest* class is responsible for increasing the average observed σ^0 with a larger spread in observed values. σ^0 over *non-irrigated arable land* has much lower values and is centered at 0.05 along with most other land cover classes, except *coniferous forest*.

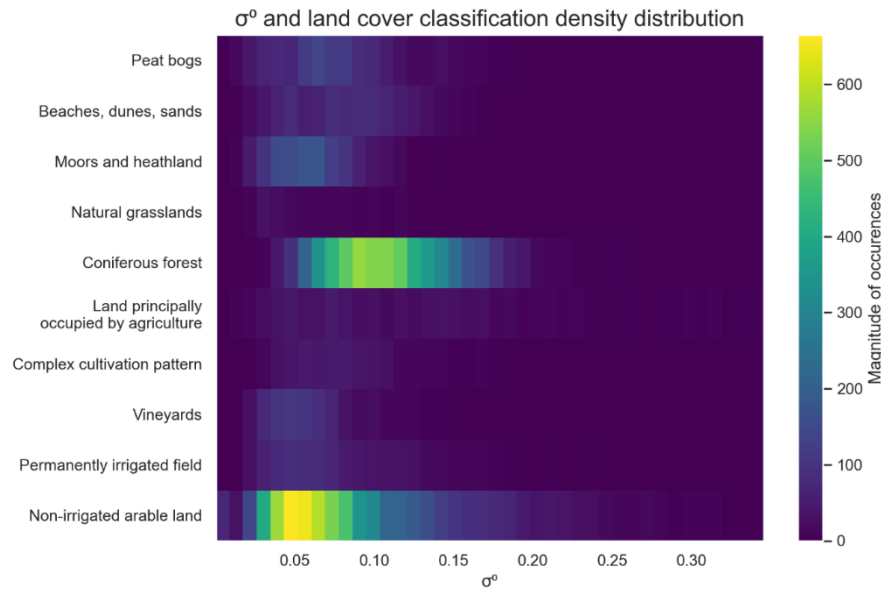


Figure 18. Density distribution of Sigma Nought (σ^0) for different land covers. Each bar represents increments in σ^0 by ~ 0.01 between 0-0.35.

The vegetation indices, NDVI and NDWI, had a weak positive linear relationship with SSM in the correlation analysis (Fig. 12). A three-dimensional representation of the relationship between SSM and NDWI (Fig. 19) shows a non-uniform distribution with a similar high magnitude of occurrences between 0-30% SSM as the Sigma distribution (Fig. 17). It is therefore possible to assume that NDWI, like σ^0 , is likely dependent on SSM but is complicated by external parameters and variables. This is further complicated by the aggregation of multiple land cover types, which have significant differences in NDWI profile under similar levels of SSM.

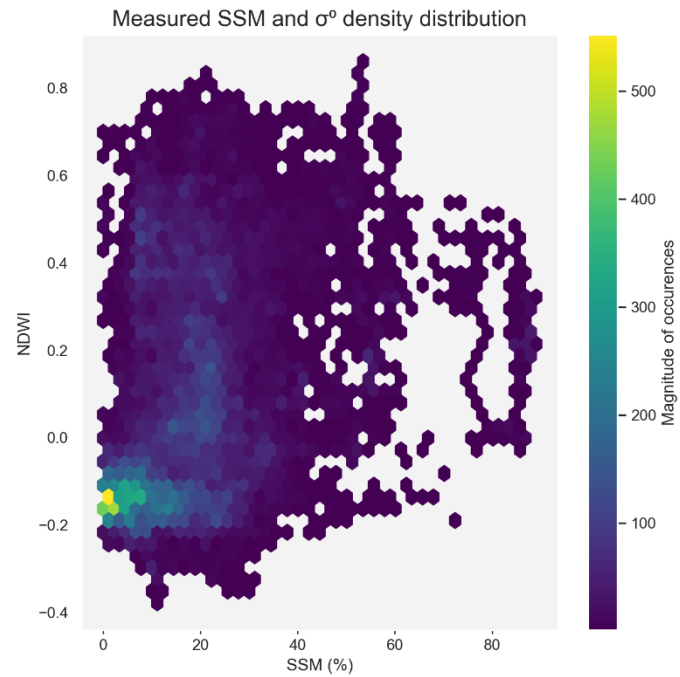


Figure 19. Density distribution of measured surface soil moisture (SSM) and Sentinel-2 derived Normalized Difference Water Index (NDWI). Each hexagon represents increments of 2.2% SSM between 0-89% and 0.03 NDWI between -0.4-0.9.

4.1.4. Time-series analysis

The interference caused by aggregating multiple land cover types from different regions can be negated by looking at a single SM probe. This is also, in theory, how the model learns statistical relationships from the variables to produce rules about predictions. For this example and going forwards, the REMEDHUS probe at ‘Casa Periles’ (*non-irrigated arable land*) has been chosen to illustrate these relationships. The Casa Periles SM probe has one of the most complete time-series’ in the dataset and belongs to the largest division of land cover/region probes. For regional variables, the *non-irrigated arable land* probes in Spain have been combined to diminish outliers without introducing noise from multiple land covers and/or regions. This combination has been chosen due to having the largest proportion of samples in the dataset and thus contributing most to the training of the network.

The linear relationship between NDVI and NDWI was determined to be $r = 0.8$ (Fig. 12) due to both VIs dependence on the same NIR band to derive spectral information. NDWI, however, shows a higher sensitivity to increases in SSM (Fig. 20). The index is a measure of the water content in vegetation and hence a lag between precipitation events or increases in SSM and higher index values is expected. This is best illustrated at the two spikes in SSM between 2017-07 and 2017-10, where moisture content rises from 5 to 20% over a short period, followed by an increase in NDWI. Both VIs show some response to these events but are largely obscured by the sample frequency of the Sentinel-2 satellite. The interpolations are not sufficient in capturing short-term variations in either NDVI or NDWI. Additionally, while rain events trigger a response in the VIs, the overall trend is governed by seasonality, with higher VI values during late winter and early spring. These seasonal variations exceed any short-term changes caused by increases in SSM.

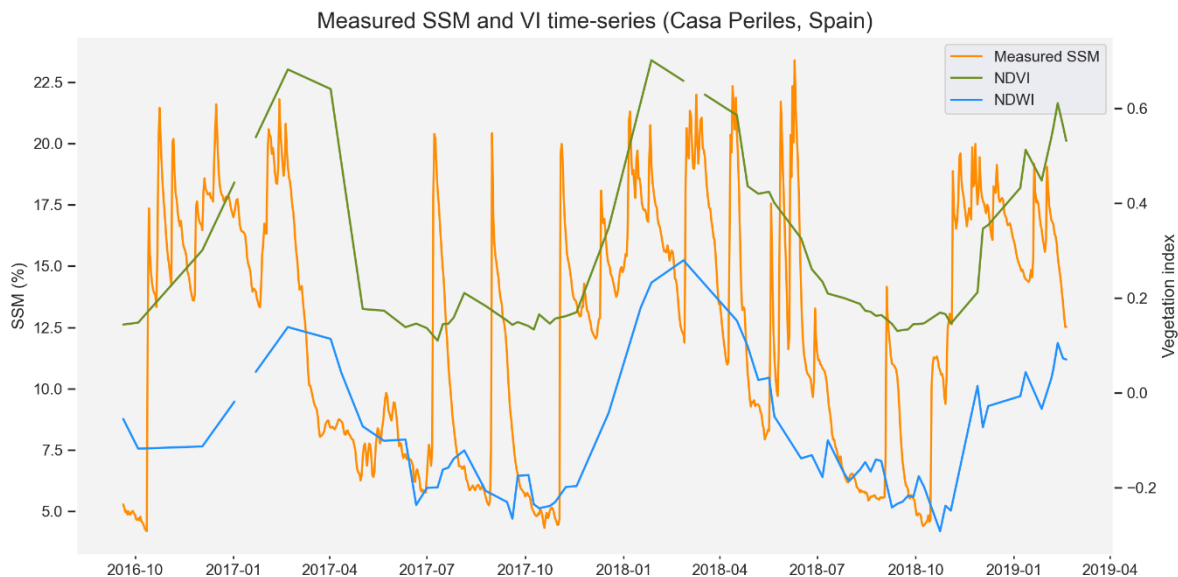


Figure 20. Time-series of measured surface soil moisture (SSM), Sentinel-2 derived Normalized Difference Vegetation Index (NDVI), and Sentinel-2 Normalized Difference (Vegetation) Water Index (NDWI) NDWI (Gao 1996) for the soil moisture (SM) probe at Casa Periles, Spain. Both vegetation indices (VI) show interpolated values from observations.

Precipitation is measured as a regional variable and the response in SSM should be reflected across all probes in the region and the median filter applied to the SM probes should diminish outliers. Here (Fig. 21), the TS_{max} shows a strong seasonal dependency, inverse of both VIs,

with a peak during summer. TS_{max} is subject to frequent short-term variations; hence the 15-day mean average of the values have been displayed with the original time-series. The TS_{max} trend displays a negative relationship with precipitation, with high temperatures during dry periods (summer) and low temperatures for periods with high SSM content (winter). Rapid spikes in SSM during the summer period are in most cases preceded by a decrease in TS_{max} by 5-10°C. Fluctuations in SSM during the winter period are not distinguishable in the TS_{max} . For precipitation, it is not clear whether there is a direct relationship with TS_{max} . The length of the time-series is likely a contributing factor as precipitation experiences more interannual variations than soil-dependent variables any may not be adequately captured within the study period. It is also difficult to ascertain whether there is any strong direct relationship between precipitation and SSM, with increases in the former only occasionally being reflected by rises in the latter.

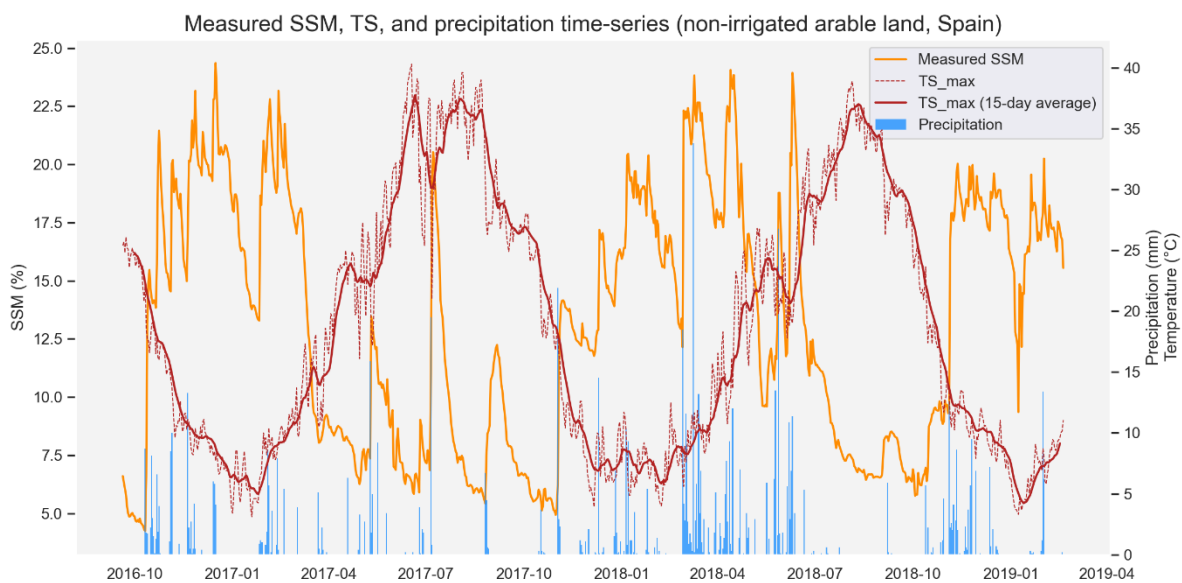


Figure 21. Time-series of measured surface soil moisture (SSM), maximum daily soil temperature (TS_{max}), and precipitation for non-irrigated arable land cover types in Spain. The 15-day average. TS_{max} has been resampled as a rolling mean over 15 days, using a negative three day offset.

4.2. Model results

4.2.1. Evaluation of land cover and region wide model results

The regional results from two of the model predictions and two external SM products (Fig. 22A) show conformity among the models and the ECV_SM product, but a large discrepancy with the CSM predictions. Denmark and Spain have the lowest errors at 6-9% MAE with both the DLM_{full} and $DLM_{minimum}$ but the error increases by +5-7% to 12-16% MAE for Sweden and an additional +7-10% to 20-25% MAE for Finland. The $DLM_{minimum}$ shows the best performance on a regional basis with an MAE of 2-5% lower than the DLM_{full} . For the ECV_SM product, the lowest error is for Denmark at 10%, while Spain and Sweden both lie at 15% and Finland at 20%. This product performs similarly to the model predictions for all regions besides Spain, where the error is 7-10% lower for the models. The CSM performs poorly overall with an MAE between 33-39% for all regions. For predictions exclusively on agricultural land cover classes (*non-irrigated arable land* and *permanently irrigated field*) (Fig.

22B) Finland has been excluded as it contains no SM probes with either of these land covers. For the remaining regions, the $DLM_{agriculture}$ shows an overall accuracy similar to the $DLM_{minimum}$. For agricultural predictions in Denmark and Spain, the three models perform equally with MAEs between 6-7% but for Sweden the DLM_{full} performs poorer at 13% MAE. All three model predictions have consistently lower MAE than the ECV_SM and CSM products.

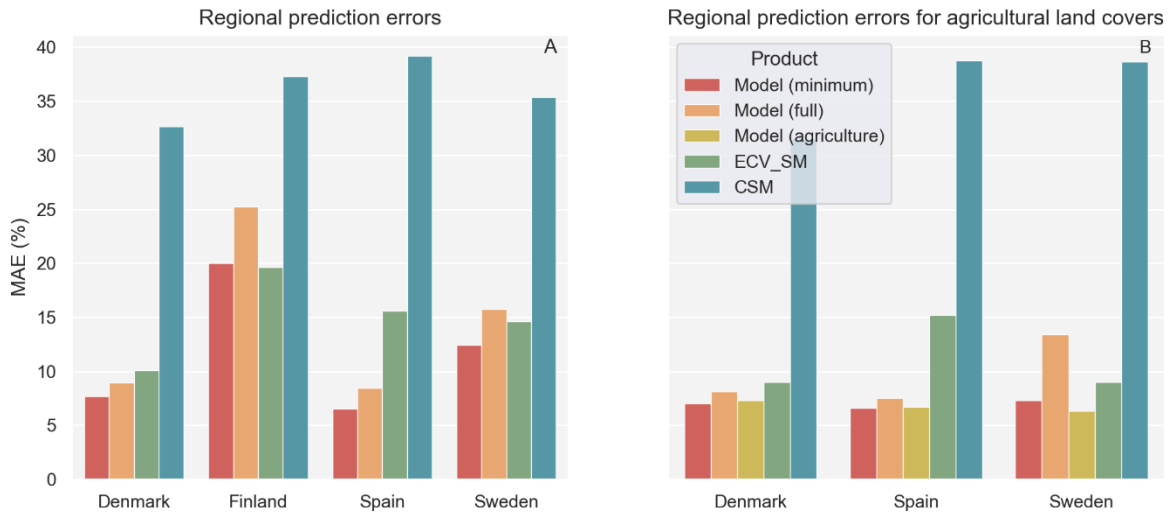


Figure 22. Mean absolute errors (MAE) at a regional scale for models and soil moisture (SM) products. Left figure (A) includes the minimum parameter model ($DLM_{minimum}$) and full model (DLM_{full}) in addition to the two SM products ECV_SM and CSM over all land cover types. The right figure (B) includes an additional model prediction, the agriculture model ($DLM_{agriculture}$). Figure (B) looks exclusively at land covers ‘non-irrigated arable land’ and ‘permanently irrigated field’.

Looking at the absolute errors across different land covers (Fig. 23) illustrates how certain land covers are associated with low accuracies or dispersed predictions. *Coniferous forest*, which is problematic for active microwaves, shows lower accuracies for both the DLM_{full} and $DLM_{minimum}$ compared to the ECV_SM. Moreover, this class has the largest spread of values and standard deviations among all the land covers. The second class, which has consistently poor predictability, is the *peat bogs*, which is underestimated by both models and SM products alike. For the remaining classes except *sand* and *land principally occupied by agriculture*, the $DLM_{minimum}$ has consistently lower absolute errors with the DLM_{full} trailing some percentages behind but mostly ahead of the ECV_SM product. There is a general trend among both models and products to overestimate SSM as evident from the spread in standard deviations in the negative. Like the regional analyses (Fig. 22), the CSM product shows poor accuracy across all land covers, with absolute errors between 0-99%.

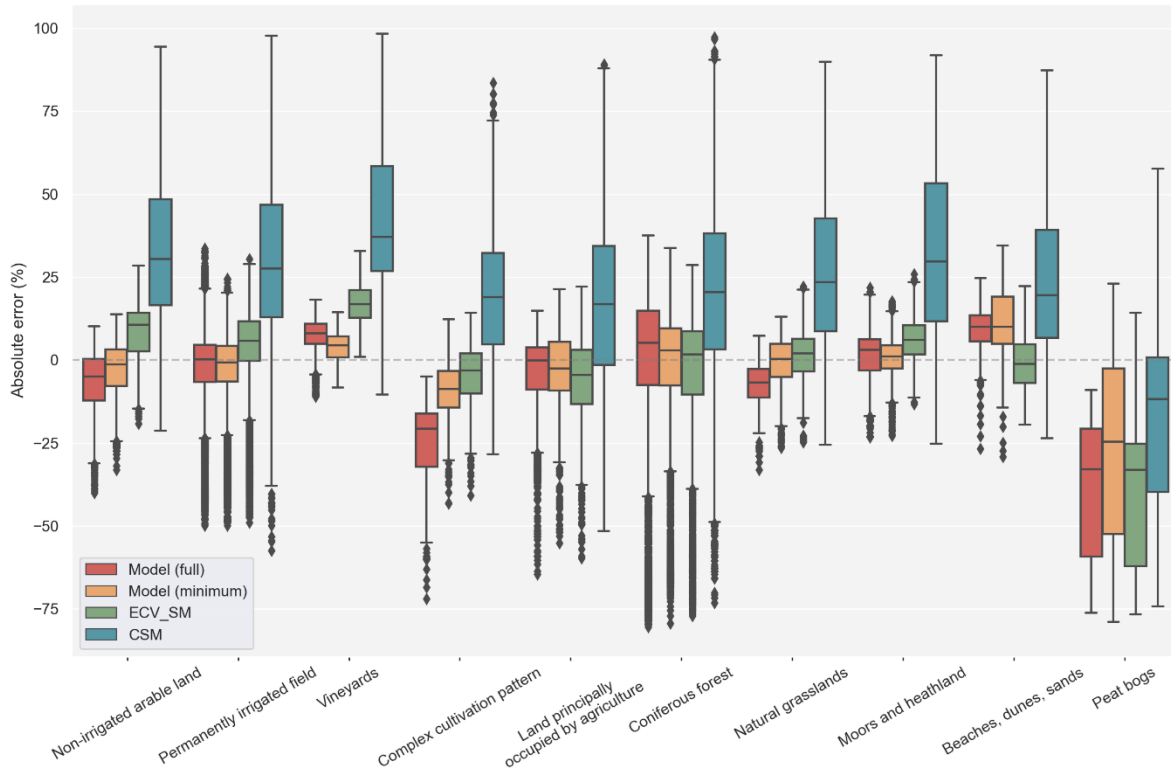


Figure 23. Distribution of absolute errors for model predictions and soil moisture (SM) products. The absolute error term is calculated as the residual between the predicted and observed surface soil moisture (SSM).

4.2.2. Comparison with existing SM products

The following scatterplots (Fig. 24) show the absolute errors of predictions from the three models tested on agricultural land covers. The models have an MAE between 6.93% ($DLM_{minimum}$) and 8.04% (DLM_{full}) and show reasonable Pearson correlation coefficients between 0.3 (DLM_{full}) and 0.48 ($DLM_{minimum}$). As corroborated by the prior results (Fig. 22 & 23) the $DLM_{minimum}$ (Fig. 24B) performs best of the three and has a lower rate of underestimations, resulting in a lower spread in values. The DLM_{full} (Fig. 24A) ranks third in both accuracy and correlation of the three and shows a stronger tendency for both under- and overestimating SSM. Unlike the $DLM_{minimum}$, the DLM_{full} occasionally gets ‘stuck’ at a zero-value prediction during training. This can also be observed to some degree in the $DLM_{agriculture}$ (Fig. 24C), which ranks slightly behind the $DLM_{minimum}$. Both the $DLM_{agriculture}$ and $DLM_{minimum}$ are trained on the same variables and differ only in the number of probes used during training. The results signify that the network is capable of ignoring conflicting inputs from other land cover classes when estimating SSM.

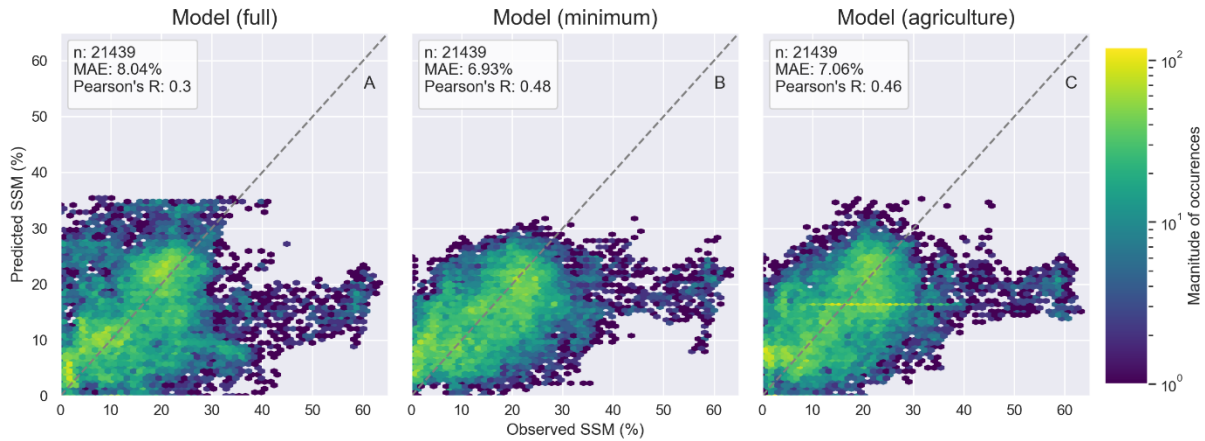


Figure 24. The relationship between observed (x-axis) and predicted (y-axis) surface soil moisture (SSM) on agricultural land covers for the (A) full model (DLM_{full}), (B) minimum (parameter) model ($DLM_{minimum}$), and (C) agriculture model ($DLM_{agriculture}$). The error term is expressed as mean absolute error (MAE) and the relationship as Pearson's correlation coefficient.

The $DLM_{minimum}$ (Fig. 25A) performs significantly better than the CSM (Fig. 25B) and slightly better than the ECV_SM (Fig. 25C) products in terms of MAE. For the correlation coefficient, the $DLM_{minimum}$ exceeds both models by 0.46 and 0.39, respectively. The ECV_SM product has a narrow spread of predictions over a wide spread of observed values, to which the opposite is true for the CSM product. Most predicted values for ECV_SM are close to the observed values with some overestimations at 5-10% but also has significant outliers for high SSM values up to 80% MAE. Similarly, the $DLM_{minimum}$ is also prone to outliers, where the observed values are above 80% SSM. Additionally, the $DLM_{minimum}$ has a cluster of errors at 60% predicted SSM for observed values at 40%, which is not present in either of the two products. The values predicted by the CSM product cluster around 40% for observed values between 0-40% SSM, which results in absolute errors in the same range. The distribution for CSM predictions is less centered than the $DLM_{minimum}$ and the ECV_SM product, which also leads to a poor correlation coefficient at 0.03. A full set of MAEs for model and product estimations are given in Appendix B.

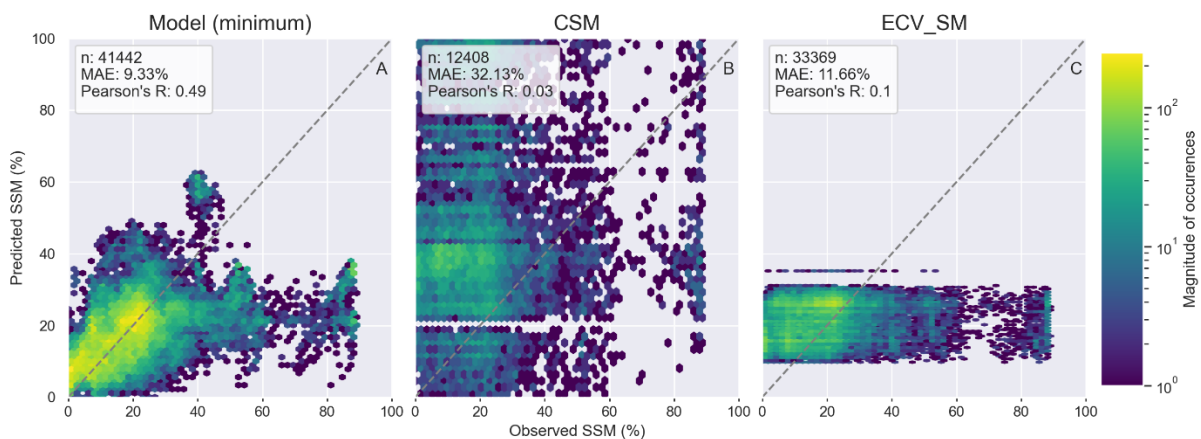


Figure 25. The relationship between observed (x-axis) and predicted (y-axis) surface soil moisture (SSM) for the (A) minimum parameter model ($DLM_{minimum}$), (B) CSM product, and (C) ECV_SM product. The error term is expressed as mean absolute error (MAE) and the relationship as Pearson's correlation coefficient.

Pivoting the scatterplots (Fig. 25) into a time-series (Fig. 26) shows the time-dependent predictions errors of the $DLM_{minimum}$ and the two SM products. The $DLM_{minimum}$ remains relatively stable throughout the study period but with some extreme negative outliers at -70%, which can also be observed in the ECV_SM time-series. The ECV_SM predictions are generally overestimating SSM by 10-20% but show seasonal variations with higher prediction errors during the winter months, which is likely a result of more saturated soils during this period. The opposite pattern is true for the CSM predictions, where the absolute error rarely reaches zero besides during later winter and early autumn. Predictions for the CSM product also favor overestimations for most of the study period. In general, the models are more likely to overestimate the SSM for most land covers, as it rarely rises above 50% moisture content. This leads to a bias towards small SSM values and hence more room for over- than underestimations. This is well captured by the CSM product, where predictions are less accurate and overestimations reach +99%, while underestimations are few and reach -75% for singular outliers.

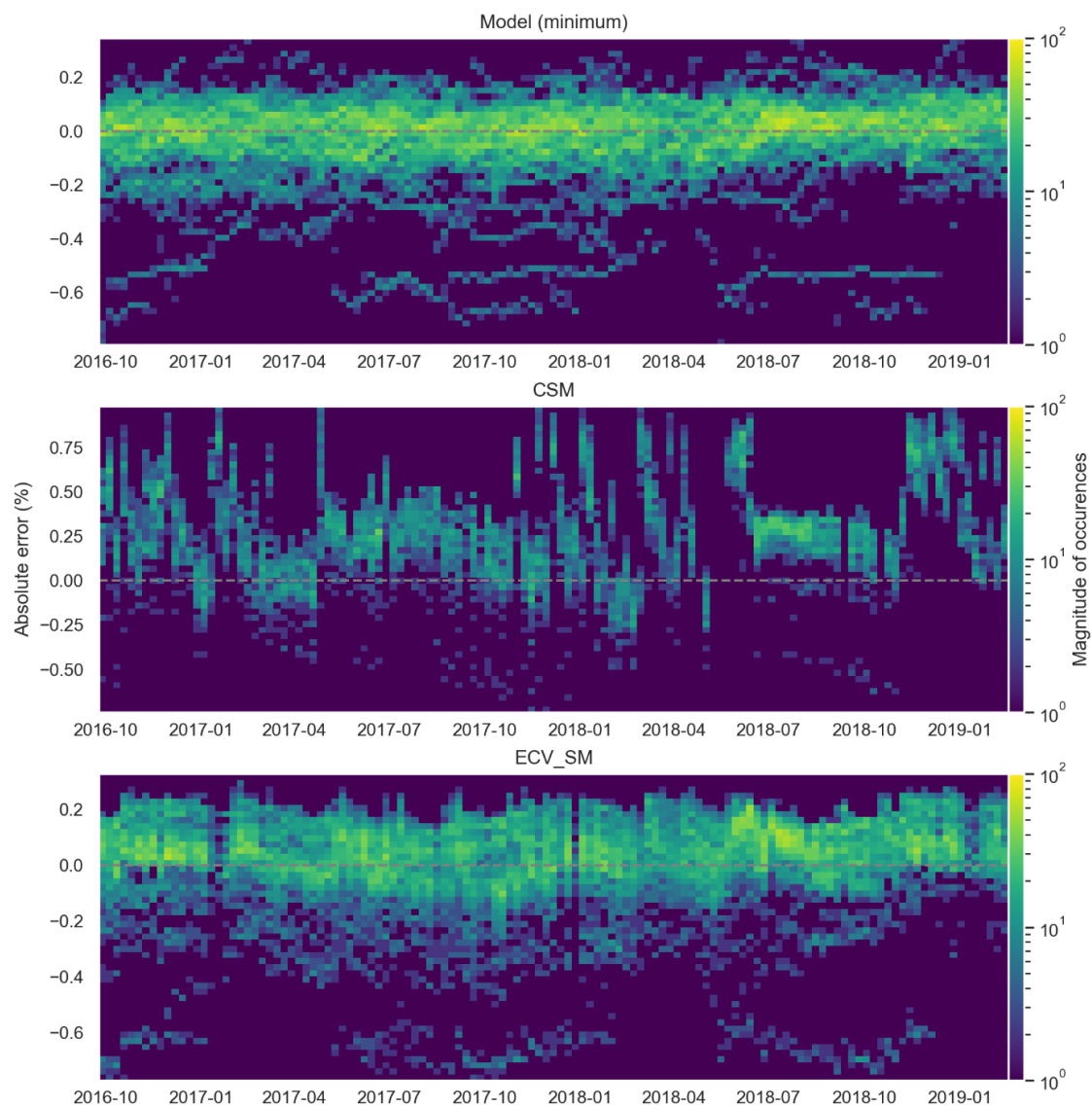


Figure 26. Surface soil moisture (SSM) prediction errors for the minimum parameter model ($DLM_{minimum}$) and the two soil moisture (SM) products, CSM and ECV_SM. Values are expressed as the absolute error between predicted and observed SSM at given dates for the soil moisture SM probe at. Each pixel corresponds to a weekly cumulative count of values.

The MAE for both models and products varies greatly for different land covers (Table 4). The $DLM_{minimum}$ exceeds the DLM_{full} in accuracy on all land covers except *beaches, dunes, sands* by 0.12% for *moors and heathland* to 13.62% for *natural grasslands*. The $DLM_{agriculture}$ scores similarly to the $DLM_{minimum}$ for both included classes in this model, with higher MAE for *non-irrigated arable land* but lower for *permanently irrigated field*. Accuracies are highest with the $DLM_{minimum}$ for the agricultural land cover classes *non-irrigated arable land, complex cultivation pattern, land principally occupied by agriculture, and permanently irrigated field* with an MAE between 4.75-6.96%. Additionally, *vineyards* also have a low MAE for this model with 4.99%. The ECV_SM product has a similar pattern with an MAE between 6.37-10.36% for the same agricultural land covers. The performance is overall slightly worse than both the $DLM_{minimum}$ and DLM_{full} for all land cover types except *beaches, dunes, sands* and *natural grasslands*. The CSM product performs poor across all land cover types but shows better performance than both DLMs and ECV_SM for *peat bogs*, which is likely due to its high rate of overestimation.

Table 4. Mean absolute errors (MAE) for the three investigated deep learning model (DLM) variations and the two existing soil moisture (SM) products, CSM and ECV_SM, over different land covers in the study area.

Land cover	DLM_{full}	$DLM_{minimum}$	$DLM_{agriculture}$	CSM	ECV_SM
Moors and heathland	0.0966	0.0954		0.2748	0.1079
Coniferous forest	0.1647	0.1274		0.3024	0.1331
Non-irrigated arable land	0.0801	0.0696	0.0722	0.3306	0.0904
Complex cultivation pattern	0.0791	0.0568		0.3003	0.0637
Land principally occupied by agriculture	0.0590	0.0475		0.3510	0.0751
Beaches, dunes, sands	0.0988	0.1241		0.2697	0.0665
Permanently irrigated field	0.0826	0.0674	0.0583	0.3439	0.1036
Peat bogs	0.3768	0.3146		0.2512	0.4093
Vineyards	0.0807	0.0499		0.4283	0.1652
Natural grasslands	0.2465	0.1103		0.2496	0.0794

4.2.3. Spatial and temporal model predictions

The $DLM_{minimum}$ can capture short-term variations in addition to long-term trends (Fig. 27). The seasonal fluctuations from high SSM in winter to low in summer are well represented by the $DLM_{minimum}$. Additionally, short-term fluctuations are in most instances reflected by the $DLM_{minimum}$ but fails to capture the amplitude of these changes, which is mostly seen during dry periods. In other cases, the amplitude is overestimated, which is more prevalent during already wet periods. Moreover, rapid changes in measured SSM are often not reflected immediately by the $DLM_{minimum}$, and often lags days or weeks behind.

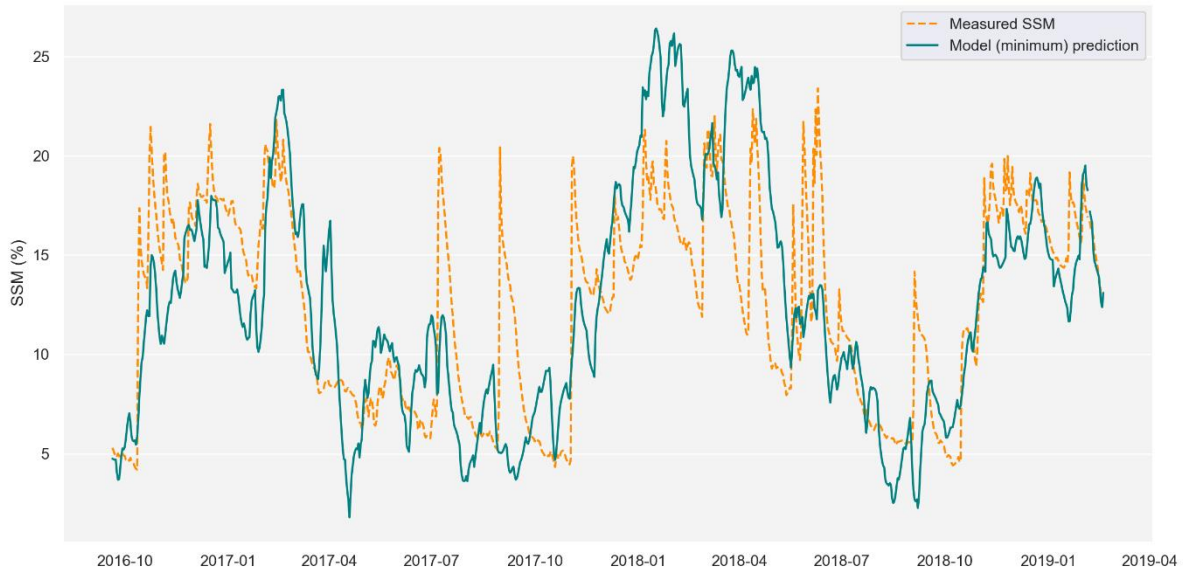


Figure 27. Model (minimum) ($DLM_{minimum}$) prediction of surface soil moisture (SSM) (solid teal) and the measured SSM used for validation (dashed orange) for the soil moisture (SM) probe at Casa Periles, Spain.

The spatial SSM predictions generated by the $DLM_{minimum}$ (Fig. 28) are constrained by the inability to assess its accuracy outside the validation probe. The predicted values do, however, fluctuate within a reasonable range (3.2-16.8%) for the area, which surrounds the validation probe ‘Casa Periles’ (Fig. 27). During the same period at the validation probe the SSM is measured at 6.5%. The spatial predictions cover an area dense in agricultural fields with different irrigation schemes and vegetation types, which leads different SSM levels at parcel levels. This is illustrated in the spatial predictions, which calculate these differences from the satellite-based indices, σ^0 , NDVI, and NDWI.

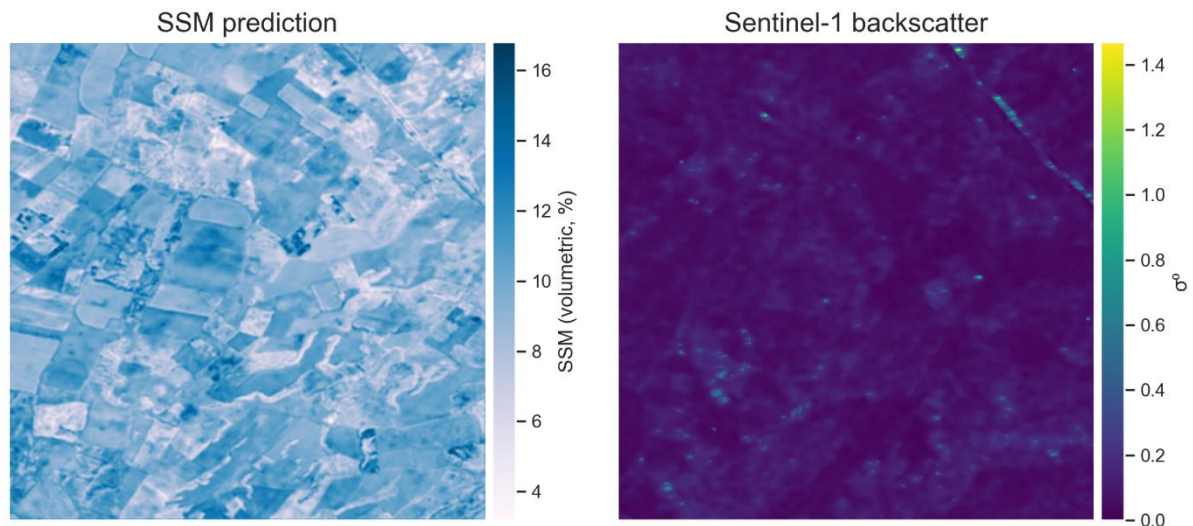


Figure 28. Spatial surface soil moisture (SSM) estimation (left) and sigma nought backscatter (right) of a 5x5 km area within the REMEDHUS study area on 2018-08-03. The validation probe ‘Casa Periles’ is located at the centroid of the image. The spatial prediction is generated with the $DLM_{minimum}$.

5. Discussion

5.1. Evaluation of existing products

The CSM product shows how empirical models may fail to adequately capture complex relationships. For the CSM product, where the model uses an assumption of saturation of both 0 and 100% SM content within an observed period, the data (Fig. 15) shows how this is unlikely to be true over most land covers. Combined with a sampling rate of 1-6 days, it becomes improbable for the sensor to capture both extremes. As a result, the model will scale values of a smaller range with the assumption that both extremes have been recorded, thus leading to both under- and overestimations of SSM. The results from this model are therefore both imprecise and inaccurate, which are reflected by the large range in standard deviations and poor MAE of 32.13%. The ECV_SM model with its combined sensor approach has an overall MAE of 11.66% and thus only slightly higher than the $DLM_{minimum}$ prediction in absolute terms, despite the much coarser resolution of the former. However, the product has no recorded predictions for SSM above ~35%, thus leading to large errors for wetter land covers, such as *peat bogs*. Similarly, the $DLM_{minimum}$ predictions have a high rate of error for extremely wet land covers at >80% SSM and a cluster of overestimations at 60% predicted SSM and 40% observed. It is most likely that these stem from the *coniferous forest* due to the high magnitude of occurrences and the known disturbance from dense vegetation. Despite the outliers, the $DLM_{minimum}$ performs better than either of the two products, CSM and ECV_SM, and the other two models, DLM_{full} and $DLM_{agriculture}$.

A study by Colliander et al. (2018) assessed the accuracy of the SMAP enhanced soil moisture product on a set of in situ probes in the continental United States and Europe. This evaluation includes the HOBE probes, where they found a root mean square difference (RMSD) of 0.012 with a correlation of $r = 0.976$ during the period April 1 2015 to April 1 2017. The SMAP product was validated on a global set of in situ measurements, including the REMEDHUS probes, prior to this assessment. Additionally, a study by Bircher et al. (2013) performed a validation of the SMOS L1C and L2 products using the HOBE probes and found an RMSE of 0.102 with a correlation of $r = 0.49$ during the year 2010. Moreover, this study also showed variation in RMSE with soil texture, where higher clay content resulted in higher RMSE, and land cover. However, most differences in RMSE over land covers resulted from varying crop types rather than land cover itself. From just the HOBE validations, the two existing SM products, SMOS and SMAP, vary in accuracy of approximately an order of magnitude. Few studies have used the FMI probes for microwave-based SM estimations, likely due to the noisy land cover classes and persistent snow and cloud cover throughout most of the year. The ICOS probes have also not been used in any microwave-based SM studies but here due to the novelty of the data rather than the quality.

5.2. Deep learning model

The DLM predictions show accuracies comparable to or better than two of the existing SM products. This indicates that DL is a suitable method in SM studies and could likely exceed many existing models in accuracy given further research. The advantages of DL are high accuracies across complex multivariate datasets, where conventional ML methods fail to extract meaningful relationships. Additionally, DL models require little expert input with

regards to the feature engineering of the inputs in the model, which may likely reduce the expert requirements normally needed for this step. However, some of the negative aspects of DL are the black box modelling, the large datasets often required, and the computing power necessary to run most algorithms efficiently. Moreover, due to the structure of RNNs, feature importance cannot be retrieved once the model has been trained and redundant, disruptive, or beneficial features cannot be easily discerned. Hence, DL is not the best solution for every ML problem, but the results presented in this thesis show that it can be a good solution regarding SAR-based SM estimations.

The spatial predictions provide a high spatial resolution estimation of SSM at 10m resolution. This is in addition to a high temporal resolution at 1 day frequency. These estimations are unvalidated but do show variations within a reasonable range from the validation probe located at the centroid. It is thus feasible to conclude that an RNN structure can generate both temporal and spatial predictions, despite only specializing in the former. The spatial capabilities are largely facilitated by the spatial data, such as σ^0 and NDVI, which are natively autocorrelated. For the DLM_{full} , the addition of static variables to the network resulted in either poor agreement with the dynamic variables, or simply too many parameters with too few samples to find meaningful relationships between. However, results were not unanimous across all validation probes and some showed better results with the DLM_{full} model than the $DLM_{minimum}$. With larger datasets these discrepancies would be more consistent between model iterations and the causes would likely be more apparent. The $DLM_{agriculture}$ performed similarly to the $DLM_{minimum}$ and the difference is likely due to the random initialization weights and validation splits during training. Because the $DLM_{minimum}$ did not perform worse than the $DLM_{agriculture}$ for agricultural land covers it shows that the network is able to adapt to the various types of SSM niches occurring across land covers and regions. That the $DLM_{agriculture}$ did not perform better than $DLM_{minimum}$ may also indicate that reducing the number of land cover classes in the dataset provides a comparable increase in accuracy as the loss of accuracy from the reduction of samples.

The generalization of the DLM was limited by the consistency and distribution of available samples. The gaps in the dynamic variable datasets were not distributed evenly for all SM probe networks and many were limited especially by cloud cover. Moreover, the geographical locations of the probes were also not distributed evenly across climate types. Hence, the DLM received an unbalanced dataset favouring some regions for certain variables and other regions for different variables.

The ancillary variables' purpose is twofold: They assist predictions of SSM by providing alternative relationships between them, σ^0 , and SSM. Secondly, they provide means of estimating SSM for periods where no backscatter data is available. This allows the network to create a full time-series of SSM during the study period, despite the limitation of only having backscatter data for half or a third of the dates. This is evident from Fig. 25A and B, where the number of predictions from the CSM dataset are 30% of the $DLM_{minimum}$ predictions. This will likely have an impact on the overall accuracy for any given data in the time-series, but further research is required to determine to what degree.

5.3. Ancillary predictive variables

Two of the most important ancillary variables that are necessary to accurately estimate SSM from microwave radar is vegetation (index) (Pariante 2002) and soil texture (Bhat et al. 2007). For most probes in the network, however, both variables were limited in either accuracy or coverage. The HOBE and ICOS networks both experienced periods of consistent cloud cover up to several months and hindering the retrieval of any vegetation indices. For the FMI probes, due to their geographic position in the far north, were greatly limited in coverage of optical satellites due to cloud and snow cover. This resulted in a very poor VI profile with only 5-10 points during the entire study period. Fortunately, this limitation did not apply to the REMEDHUS probes, where it was possible to get a consistent optical coverage due to a combination of better sampling frequency by the Sentinel-2 satellite and fewer clouds. However, considering the qualitative relationship between the NDVI/NDWI and SSM (Fig. 20), the importance of these variables in the model is doubtful. Both variables have a lag component in relation to SSM and are more informative about antecedent conditions rather than current or future conditions. Other studies have used NDVI as a masking component to eliminate problematic areas (Gao et al. 2017) or compensate for the attenuation caused by the vegetation (Alexakis et al. 2017). A similar approach may be beneficial to the DLM, where areas of dense vegetation are masked out prior to training to reduce noise in the dataset. The importance of soil texture in the DLM was severely diminished by the spatial resolution of the data at 30 arc-seconds, which failed to accurately reflect soil texture at individual SM probes. Hence, many probes with different soil textures were assumed by the DLM to be identical and erroneous relationships were created between responses in SSM for given soil textures. This is likely one of the reasons why the $DLM_{minimum}$ performed better than the DLM_{full} overall.

Changes in SSM are strongly linked to precipitation with most variations in the former being explained by events of the latter, hence the motivation for including precipitation as a variable in the DLM. Precipitation is subject to strong local variations in both intensity and frequency, especially during the hotter months. For this reason, it is important, when considering precipitation as an ancillary predictor, to aim for the highest accuracy of measurements. Rain gauges provide one of the most accurate point-based measurements of precipitation with low bias and few random errors compared to satellite or radar products (Wagner et al. 2003; Sun et al. 2018). With a mean distance of <45 km from every SM probe in each study area to the respective weather, it is likely that weather stations will provide higher accuracies than both radar and satellite products. However, at this distance and from the distance between points within study areas, it can also be assumed that there will be heterogeneity in precipitation patterns between SM probes. These inter-probe variations are not captured in the precipitation data but will show up in the SSM measurements, which will result in conflicting relationships in the network. This will have a higher consequence in dry and hot regions or periods, where precipitation is likely to experience greater local variations and affect the SSM more severely.

TA is also an important modulator of SSM but does not experience the same local variability as precipitation. Moreover, the correlations between TA and TS were $r = 0.9$ for all types of TA, but $r = 0.4$ between TA_{mean}/TA_{max} and SSM, and $r = 0.5$ for TS_{max} and SSM. While TS_{max} and TA are closely correlated, the relationship with SSM is better explained by TS_{max} .

It is then likely that scaling the model up for areas not covered by SM/TS probes would result in a slight decrease in overall accuracy.

5.4. Soil moisture variations by land cover and region

Both the $DLM_{minimum}$ and DLM_{full} showed higher MAE for less represented and unique land covers and regions. This is unfortunately one of the limitations of deep learning, where representation in the model is roughly equal to the size of the input. Due to the heterogeneity of SM across land covers of various vegetation coverages, surface roughness parameters, and soil textures, the DLM would require far larger datasets to accurately estimate SM for all land covers in the dataset. For the land covers with the highest representation of samples the MAEs were 6.96% and 12.74% for *non-irrigated arable land* and *coniferous forest*, respectively. However, some plots exhibited outliers up to 48.35% MAE but with nearby plots in the same network and on the same land cover type with MAEs of 7.25%. Hence, not only the quantity of data will be a determining factor in ability of the network to estimate SSM but also the quality. These extreme outliers, which exist for several land cover types in the dataset, likely have externally contributing factors, which make them more difficult for the network to interpret. This may be a unique soil texture giving the soil a distinct spectral profile or dense vegetation obscuring the probe. These issues are not immediately distinguishable from the input dataset and thus care should be taken to examine the output of the model with respect to individual probes.

Peat bogs were only represented by two ICOS probes and an FMI probes but are responsible for most of the outliers in the DLM predictions. Other studies (Dorigo et al. 2015) have removed measurements taken in *peat bogs* from the dataset as they contaminate the microwave signal (Draper et al. 2012). They were included in this study to test if the ancillary variables would be able to mask out the poor quality σ^0 backscatter signals received. It appears from the estimations in *peat bogs*, that this was not successful. This task was further complicated by the lack of Sentinel-2 coverage at the study sites due to persistent cloud and snow cover and was thus limited to temperature and precipitation.

DLM predictions for *coniferous forest* were generally acceptable but contained many outlying predictions. Both the $DLM_{minimum}$ and DLM_{full} had underestimations up to -80%, which also raises some further questions about the quality of the data from the SM probes during these intervals of extremely high moisture contents. Previous studies (Moran et al. 2000; Wagner et al. 2003) have established a strong attenuation of microwave signals, and especially shorter wavelengths, over vegetated areas. In addition to attenuating the soil backscatter the vegetation also provides its own backscatter (He et al. 2014) and introduces noise in the signal. For the VV-polarization the backscatter signal from soil dominates the vegetation backscatter until approximately 0.8 NDVI (El Hajj et al. 2017), which is generally observed over forests during spring and summer. Hence, it is possible to extract some information about SSM from the σ^0 , which is evident from the MAE at 12.74% for *coniferous forests*. Given a complete time-series of NDVI it would have been possible to further mask out periods with too high NDVI for better DLM predictions.

For a larger dataset with better distribution of land cover classes, it would have been possible to separate SM probes based on spectral or physical features prior to training. It can be argued

that introducing the static variables to the DLM led to lower generalization from having to fit the weights to more features. Moreover, with the coarse resolution provided for the soil data at 30 arc-seconds, most probes within each network were considered similar in terms of soil texture, which is unlikely at this scale. It may thus be beneficial to perform a clustering of probes based on these variables prior to training and then construct a network for each cluster independently. This would require a larger dataset for proper representation of each class but would likely lead to better results.

The regional differences in SSM predictions are between 2-3% MAE for Denmark and Spain with the highest MAE for the former. This can be attributed to two SM probes in the HOBE network, which have MAEs exceeding the median error of the network predictions by 16.42% and 26.09% on *coniferous forest* and *non-irrigated arable land*, respectively. For Finland and Sweden, where the regional MAEs exceed Denmark and Spain by 8-17%, the errors are linked to the types of land covers, which are mostly limited to *coniferous forest* and *peat bogs*. Coupled with the low number of samples and poor Sentinel-2 coverage, the DLM is unable to create enough relationships between the variables and thus leads to poor accuracy in the predictions.

5.5. Critical reflections on the accuracy of surface soil moisture

The accuracy of the predictions below 5% SSM conflict with the technological limits imposed by the equipment used for validation. The SM probes used at the study sites have a 2-5% accuracy baseline (Susha Lekshmi et al. 2014; Bellingham 2015; Caldwell et al. 2018) if the sensor has been both site- and soil-calibrated. Readings above 5% SSM would likely cancel out and thus the critical aspect of the accuracy only concerns the bottom 5%. If the sensors do not provide accurate readings, the model will associate the given backscatter value with the reported SSM, which would propagate the errors throughout the network.

For agricultural land cover types the measured SSM occasionally surpassed 50% and for *coniferous forest* and *peat bogs* this occurred much more frequently. Rao and Singh (2011) established that measurements by SM probes are limited to $\leq 50\%$ moisture content, which raises some questions about the quality of the data at these intervals. Incidentally, these observations also contribute to a higher overall MAE for all the predictions and thus lowering the calculated accuracy of the DLM. It is therefore recommended that the output of the model be inspected carefully after training to detect where and why it fails to estimate SSM for specific probes or periods.

5.6. Future work

The results presented in this thesis are primarily concerned with point-based results, where the predictions can be validated. The spatial predictions generated lack a component in the architecture to increase precision by using neighboring pixels. It is then likely, that combining RNN layers with 2D convolutions may provide better results at a spatial scale. Some recent work has used these combinations, aptly named Temporal Convolutional Neural Network or TempCNN/TCN, for classification of satellite image time-series (Pelletier et al. 2019) and spatial weather prediction (Hewage et al. 2020). This architecture is likely to perform well for SSM estimation due to both the spatial and temporal component of the variable but will also require greater amounts of in situ data for training and validation. The current model could also

be used to gap-fill existing SSM records with minor changes to the algorithm but is outside the scope of this thesis. This is one of the most common applications for RNNs as they excel in predicting vectors or sequences from sequence data (Malhotra et al. 2017; Wan et al. 2019) and should be explored further.

Few studies are concerned with SSM estimations below 1 km spatial resolution and even fewer consider the temporal component of this, which makes it difficult to evaluate the spatial predictions for similar results. However, in this context it is important to consider that spatial predictions cannot inherently be validated against in situ data, which may be considered the ground truth. Despite this there are still methods to achieve a more reliable evaluation metric of the spatial predictions. One solution would be testing the model using an area unknown to the model, which contains several probes on various land covers. Another suggestion would be to test the performance of different architectures or traditional ML methods to see how the RNN structure compares.

The DLM relies exclusively on VV-polarized backscatter and hence the results from other polarizations or the inclusion of multiple polarizations have not been explored. Other studies (Paloscia et al. 2013; Baghdadi et al. 2016; El Hajj et al. 2016; Gao et al. 2017; El Hajj et al. 2017) have used the same or different polarizations with varying results and one can therefore not be exclusively determined better than the other for SSM estimation. There is some evidence (Karjalainen et al. 2004; Patel et al. 2006; Gao et al. 2017) that suggests the VV-polarization is less susceptible to vegetation cover and may thus be more suitable for areas with higher NDVI. Meanwhile, other polarizations may give better results for non-vegetated surfaces.

The point-wise extraction of values used for preprocessing the spatial data to time-series makes it simple to scale the model up for larger areas but introduces an uncertainty component due to the noisy backscatter signal. It may be beneficial during the training stage to use plot-wise SSM averages over agricultural fields and forest stands to reduce the noise component. This will likely lower the precision of the predictions but give higher accuracies.

MAE is not a commonly used evaluation metric within remote sensing-based SM studies despite its ease of interpretation. RMSE is more commonly used, which makes it difficult to compare the results between this study and others with similar focus that use RMSE. In cases where the SM products are available and cover the same validation areas, the results can be compared directly. However, few SM datasets with equally high spatial and temporal resolution are publicly available. It may thus be useful to consider additional metrics when evaluating the results of the model predictions to create a product more easily comparable with other solutions.

6. Conclusions

The aim of this thesis was to develop and evaluate a deep learning-based method to estimate SSM at high spatial and temporal resolution across multiple land cover and climate types. This was initialized with the development of a pipeline to process the data efficiently and automatically into a homogenous multivariate dataset. A Recurrent Neural Network (RNN) built on Long-Short Term Memory (LSTM) cells was developed to estimate SSM from a multivariate dataset including Sentinel-1 C-band SAR, Sentinel-2 NDVI/NDWI, soil texture,

meteorological data, and topographic indices. Variables were observed during a study period from 2016-09-20 to 2019-02-19, or 883 days across 61 SM probes located in Denmark (HOBE), Spain (REMEDHUS), Finland (FMI), and Sweden (ICOS). The deep learning model (DLM) showed comparatively lower mean absolute errors (MAE) than two existing SSM products: The ECV_SM developed as a global SSM model from active and passive sensors, and CSM that uses empirical transformations of per-pixel statistics of Sentinel-1 data to derive SSM. Three types of model configurations were tested, where the $DLM_{minimum}$ showed the lowest prediction error and highest correlation with observed values. MAEs were lowest for *agricultural land covers* (4.75-6.96%) and highest for *peat bogs* (31.46%) and *coniferous forest* (12.74%). Overall, the MAEs of the $DLM_{minimum}$, ECV_SM, and CSM were 9.33%, 11.66%, and 32.13% between predicted and observed values from in situ measurements. Additionally, the DLM predicted near complete time-series of SSM estimations for all probes, where predictions could be validated due to the inclusion of ancillary variables. This contrasts with microwave-exclusive SM products that only provide estimations where backscatter data is available. The DLM was limited by an uneven distribution of data across the different regions and climate types, which led to poorer generalization between probe networks. Some networks had a higher representation of certain variables than others, which likely contributed to this issue. Despite the limitations the DLM produced SSM estimations for SM probes, which were comparable to or better than existing SSM products.

Because of the pipeline built to automate the processing workflow, this model can be scaled up or down for any number of probes and regions. It is fully compatible with measured SM products from both ISMN and ICOS and data in raster, shapefile, or CSV format. It also includes a post-processing verification algorithm for extracting values from existing SM products for comparison in either NetCDF or raster format. The full pipeline and model are accessible at <https://github.com/nicklts/RNN-SM-Model>.

References

- Abbaszadeh, P., H. Moradkhani, and X. Zhan. 2019. Downscaling SMAP Radiometer Soil Moisture Over the CONUS Using an Ensemble Learning Method. *Water Resources Research* 55: 324–344. doi:10.1029/2018WR023354.
- Abowarda, A. S., L. Bai, C. Zhang, D. Long, X. Li, Q. Huang, and Z. Sun. 2021. Generating surface soil moisture at 30 m spatial resolution using both data fusion and machine learning toward better water resources management at the field scale. *Remote Sensing of Environment* 255. Elsevier Inc. doi:10.1016/j.rse.2021.112301.
- Adeyemi, O., I. Grove, S. Peets, Y. Domun, and T. Norton. 2018. Dynamic neural network modelling of soil moisture content for predictive irrigation scheduling. *Sensors (Switzerland)* 18. doi:10.3390/s18103408.
- Ahmad, S., A. Kalra, and H. Stephen. 2010. Estimating soil moisture using remote sensing data: A machine learning approach. *Advances in Water Resources* 33. Elsevier Ltd: 69–80. doi:10.1016/j.advwatres.2009.10.008.
- Alexakis, D. D., F. D. K. Mexis, A. E. K. Vozinaki, I. N. Daliakopoulos, and I. K. Tsanis. 2017. Soil moisture content estimation based on Sentinel-1 and auxiliary earth observation products. A hydrological approach. *Sensors (Switzerland)* 17: 1–16. doi:10.3390/s17061455.
- Ali, I., F. Greifeneder, J. Stamenkovic, M. Neumann, and C. Notarnicola. 2015. Review of machine learning approaches for biomass and soil moisture retrievals from remote sensing data. *Remote Sensing* 7: 16398–16421. doi:10.3390/rs71215841.
- Ali, I., S. Cao, V. Naeimi, C. Paulik, and W. Wagner. 2018. Methods to Remove the Border Noise from Sentinel-1 Synthetic Aperture Radar Data: Implications and Importance for Time-Series Analysis. *IEEE Journal of Selected Topics in Applied Earth Observations and Remote Sensing* 11: 777–786. doi:10.1109/JSTARS.2017.2787650.
- Babaeian, E., M. Sadeghi, T. E. Franz, S. Jones, and M. Tuller. 2018. Mapping soil moisture with the OPTical TRAppezoid Model (OPTRAM) based on long-term MODIS observations. *Remote Sensing of Environment* 211. Elsevier: 425–440. doi:10.1016/j.rse.2018.04.029.
- Baghdadi, N., N. Holah, and M. Zribi. 2006. Calibration of the Integral Equation Model for SAR data in C-band and HH and VV polarizations. *International Journal of Remote Sensing* 27: 805–816. doi:10.1080/01431160500212278.
- Baghdadi, N., R. Cresson, M. El Hajj, R. Ludwig, and I. La Jeunesse. 2012. Estimation of soil parameters over bare agriculture areas from C-band polarimetric SAR data using neural networks. *Hydrology and Earth System Sciences* 16: 1607–1621. doi:10.5194/hess-16-1607-2012.
- Baghdadi, N., M. El Hajj, and M. Zribi. 2016. Coupling SAR C-band and optical data for soil moisture and leaf area index retrieval over irrigated grasslands. *International Geoscience and Remote Sensing Symposium (IGARSS)* 2016-Novem: 3551–3554. doi:10.1109/IGARSS.2016.7729919.
- Balenzano, A., G. Satalino, V. Pauwels, and F. Mattia. 2011. Soil moisture retrieval from dense temporal series of C-band SAR data over agricultural sites. *International Geoscience and Remote Sensing Symposium (IGARSS)* 4. IEEE: 3136–3139. doi:10.1109/IGARSS.2011.6049883.
- Bauer-Marschallinger, B., C. Paulik, S. Hochstöger, T. Mistelbauer, S. Modanesi, L. Ciabatta, C. Massari, L. Brocca, et al. 2018. Soil moisture from fusion of scatterometer and SAR: Closing the scale gap with temporal filtering. *Remote Sensing* 10: 1–26. doi:10.3390/rs10071030.
- Bauer-Marschallinger, B., V. Freeman, S. Cao, C. Paulik, S. Schaufler, T. Stachl, S. Modanesi, C. Massari, et al. 2019. Toward Global Soil Moisture Monitoring with Sentinel-1: Harnessing Assets and Overcoming Obstacles. *IEEE Transactions on Geoscience and Remote Sensing* 57. IEEE: 520–539. doi:10.1109/TGRS.2018.2858004.
- Bellingham, B. K. 2015. *The Hydra Probe® Soil Sensor. Precision Agriculture*. Stevens Water Monitoring Systems, Inc.
- Bhat, S., D. L. Roberts, M. J. Nelson, C. L. Isbell, and M. Mateas. 2007. A Globally Optimal Algorithm

- for TTD-MDPs. In *Proceedings of the 6th International Joint Conference on Autonomous Agents and Multiagent Systems*. AAMAS '07. New York, NY, USA: Association for Computing Machinery. doi:10.1145/1329125.1329367.
- Bircher, S., N. Skou, and Y. H. Kerr. 2013. Validation of SMOS L1C and L2 Products and Important Parameters of the Retrieval Algorithm in the Skjern River Catchment, Western Denmark. *IEEE Transactions on Geoscience and Remote Sensing* 51: 2969–2985. doi:10.1109/TGRS.2012.2215041.
- Boisvert, J. B., Q. H. J. Gwyn, B. Brisco, D. J. Major, and R. J. Brown. 1995. Evaluation of Soil Moisture Estimation Techniques and Microwave Penetration Depth for Radar Applications. *Canadian Journal of Remote Sensing* 21. Taylor & Francis: 110–123. doi:10.1080/07038992.1995.10874606.
- Büttner, G., B. Kostztra, T. Soukup, A. Sousa, and T. Langanke. 2017. *CLC2018 Technical Guidelines*. Copernicus.
- Caldwell, T. G., T. Bongiovanni, M. H. Cosh, C. Halley, and M. H. Young. 2018. Field and Laboratory Evaluation of the CS655 Soil Water Content Sensor. *Vadose Zone Journal* 17: 170214. doi:10.2136/vzj2017.12.0214.
- Campbell Scientific. 2021. CS655 - 12 cm Soil Moisture and Temperature Sensor.
- Centro Nacional de Información Geográfica. 2021. Modelo Digital del Terreno - MDT05. <http://centrodedescargas.cnig.es/CentroDescargas/catalogo.do?Serie=LIDAR>. Accessed May 19.
- Chang, D. H., and S. Islam. 2000. Estimation of soil physical properties using remote sensing and artificial neural network. *Remote Sensing of Environment* 74: 534–544. doi:10.1016/S0034-4257(00)00144-9.
- Che, Z., S. Purushotham, K. Cho, D. Sontag, and Y. Liu. 2018. Recurrent Neural Networks for Multivariate Time Series with Missing Values. *Scientific Reports* 8. Springer US: 1–12. doi:10.1038/s41598-018-24271-9.
- Cho, K., B. Van Merriënboer, C. Gulcehre, D. Bahdanau, F. Bougares, H. Schwenk, and Y. Bengio. 2014. Learning phrase representations using RNN encoder-decoder for statistical machine translation. *EMNLP 2014 - 2014 Conference on Empirical Methods in Natural Language Processing, Proceedings of the Conference*: 1724–1734. doi:10.3115/v1/d14-1179.
- Chollet, F. 2018. *Deep Learning with Python*. Edited by Christina Taylor, Jerry Gaines, Aleksandar Dragosavljević, Tiffany Taylor, Katie Tennant, Alex Ott, Richard Tobias, and Dottie Marsico. First. New York: Manning Publications Co.
- Chollet, F. 2020. Keras 2.4.0.
- Colliander, A., T. J. Jackson, S. K. Chan, P. O'Neill, R. Bindlish, M. H. Cosh, T. Caldwell, J. P. Walker, et al. 2018. An assessment of the differences between spatial resolution and grid size for the SMAP enhanced soil moisture product over homogeneous sites. *Remote Sensing of Environment* 207: 65–70. doi:10.1016/j.rse.2018.02.006.
- Danish Meteorological Institute. 2016. Klimanormaler for Danmark.
- Das, N. N., D. Entekhabi, R. S. Dunbar, M. J. Chaubell, A. Colliander, S. Yueh, T. Jagdhuber, F. Chen, et al. 2019. The SMAP and Copernicus Sentinel 1A/B microwave active-passive high resolution surface soil moisture product. *Remote Sensing of Environment* 233. doi:10.1016/j.rse.2019.111380.
- Delta-T Devices Ltd. 1998. Delta - T Devices - ML2 User manual: 23.
- Dorigo, W., W. Wagner, C. Albergel, F. Albrecht, G. Balsamo, L. Brocca, D. Chung, M. Ertl, et al. 2017. ESA CCI Soil Moisture for improved Earth system understanding: State-of-the art and future directions. *Remote Sensing of Environment* 203. Elsevier Inc.: 185–215. doi:10.1016/j.rse.2017.07.001.
- Dorigo, W. A., W. Wagner, R. Hohensinn, S. Hahn, C. Paulik, A. Xaver, A. Gruber, M. Drusch, et al. 2011. The International Soil Moisture Network: A data hosting facility for global in situ soil

- moisture measurements. *Hydrology and Earth System Sciences* 15: 1675–1698. doi:10.5194/hess-15-1675-2011.
- Dorigo, W. A., A. Xaver, M. Vreugdenhil, A. Gruber, A. Hegyiová, A. D. Sanchis-Dufau, D. Zamojski, C. Cordes, et al. 2013. Global Automated Quality Control of In Situ Soil Moisture Data from the International Soil Moisture Network. *Vadose Zone Journal* 12: vzj2012.0097. doi:10.2136/vzj2012.0097.
- Dorigo, W. A., A. Gruber, R. A. M. De Jeu, W. Wagner, T. Stacke, A. Loew, C. Albergel, L. Brocca, et al. 2015. Evaluation of the ESA CCI soil moisture product using ground-based observations. *Remote Sensing of Environment* 162. Elsevier Inc.: 380–395. doi:10.1016/j.rse.2014.07.023.
- Draper, C. S., R. H. Reichle, G. J. M. De Lannoy, and Q. Liu. 2012. Assimilation of passive and active microwave soil moisture retrievals. *Geophysical Research Letters* 39: 1–5. doi:10.1029/2011GL050655.
- Engman, T., P. C. Dubois, and J. van Zyl. 1995. Corrections to “Measuring Soil Moisture with Imaging Radars.” *IEEE Transactions on Geoscience and Remote Sensing* 33: 915–926. doi:10.1109/TGRS.1995.477194.
- Entekhabi, D., E. G. Njoku, P. E. O’Neill, K. H. Kellogg, W. T. Crow, W. N. Edelstein, J. K. Entin, S. D. Goodman, et al. 2015. The soil moisture active passive (SMAP) mission. *Proceedings of the IEEE* 98. IEEE.
- European Environmental Agency. 2018. CLC 2018. *Copernicus*.
- European Space Agency. 2015. *Sentinel-2 User Handbook*.
- European Space Agency. 2019. SNAP 7.0.0.
- Filipponi, F. 2019. Sentinel-1 GRD Preprocessing Workflow. *Multidisciplinary Digital Publishing Institute Proceedings* 18: 11. doi:10.3390/ecrs-3-06201.
- Finnish Meteorological Institute. 2021. Temperature and precipitation statistics from 1961 onwards. <https://en.ilmatieteenlaitos.fi/statistics-from-1961-onwards>. Accessed May 10.
- Fischer, G., F. Nachtergaele, S. Prieler, H. T. van Velthuizen, L. Verelst, and D. Wiberg. 2008. Global Agro-ecological Zones Assessment for Agriculture. *GAEZ*.
- Gao, B. C. 1996. NDWI - A normalized difference water index for remote sensing of vegetation liquid water from space. *Remote Sensing of Environment* 58: 257–266. doi:10.1016/S0034-4257(96)00067-3.
- Gao, Q., M. Zribi, M. J. Escorihuela, and N. Baghdadi. 2017. Synergetic use of sentinel-1 and sentinel-2 data for soil moisture mapping at 100 m resolution. *Sensors (Switzerland)* 17. doi:10.3390/s17091966.
- Géron, A. 2019. *Hands-on Machine Learning with Scikit-Learn, Keras, and TensorFlow*. Edited by Rachel Roumeliotis and Nicole Tache. Second. Sebastopol, CA: O’Reilly Media, Inc.
- Gers, F. A., J. Schmidhuber, and F. Cummins. 2000. Learning to forget: Continual prediction with LSTM. *Neural Computation* 12: 2451–2471. doi:10.1162/089976600300015015.
- Google. 2020. TensorFlow 2.4.0.
- Gruber, A., T. Scanlon, R. Van Der Schalie, W. Wagner, and W. Dorigo. 2019. Evolution of the ESA CCI Soil Moisture climate data records and their underlying merging methodology. *Earth System Science Data* 11: 717–739. doi:10.5194/essd-11-717-2019.
- El Hajj, M., N. Baghdadi, M. Zribi, G. Belaud, B. Cheviron, D. Courault, and F. Charron. 2016. Soil moisture retrieval over irrigated grassland using X-band SAR data. *Remote Sensing of Environment* 176. Elsevier Inc.: 202–218. doi:10.1016/j.rse.2016.01.027.
- El Hajj, M., N. Baghdadi, M. Zribi, and H. Bazzi. 2017. Synergic use of Sentinel-1 and Sentinel-2 images for operational soil moisture mapping at high spatial resolution over agricultural areas. *Remote Sensing* 9: 1–28. doi:10.3390/rs9121292.
- El Hajj, M., N. Baghdadi, H. Bazzi, and M. Zribi. 2019. Penetration analysis of SAR signals in the C

- and L bands for wheat, maize, and grasslands. *Remote Sensing* 11: 22–24. doi:10.3390/rs11010031.
- Hassan-Esfahani, L., A. Torres-Rua, A. Jensen, and M. McKee. 2015. Assessment of surface soil moisture using high-resolution multi-spectral imagery and artificial neural networks. *Remote Sensing* 7: 2627–2646. doi:10.3390/rs70302627.
- He, B., M. Xing, and X. Bai. 2014. A synergistic methodology for soil moisture estimation in an alpine prairie using radar and optical satellite data. *Remote Sensing* 6: 10966–10985. doi:10.3390/rs61110966.
- Le Hégarat-Masclé, S., M. Zribi, F. Alem, A. Weisse, and C. Loumagne. 2002. Soil moisture estimation from ERS/SAR data: Toward an operational methodology. *IEEE Transactions on Geoscience and Remote Sensing* 40: 2647–2658. doi:10.1109/TGRS.2002.806994.
- Hewage, P., A. Behera, M. Trovati, E. Pereira, M. Ghahremani, F. Palmieri, and Y. Liu. 2020. Temporal convolutional neural (TCN) network for an effective weather forecasting using time-series data from the local weather station. *Soft Computing* 24. Springer Berlin Heidelberg: 16453–16482. doi:10.1007/s00500-020-04954-0.
- Hochreiter, S., and J. Schmidhuber. 1997. Long Short-Term Memory. *Neural Computation* 9: 1735–1780. doi:10.1162/neco.1997.9.8.1735.
- Hoerl, A. E., and R. W. Kennard. 1970. Ridge Regression: Biased Estimation for Nonorthogonal Problems. *Technometrics* 12. Taylor & Francis: 55–67. doi:10.1080/00401706.1970.10488634.
- Hu, Z., L. Xu, and B. Yu. 2018. Soil moisture retrieval using convolutional neural networks: Application to passive microwave remote sensing. *International Archives of the Photogrammetry, Remote Sensing and Spatial Information Sciences - ISPRS Archives* 42: 583–586. doi:10.5194/isprs-archives-XLII-3-583-2018.
- Im, J., S. Park, J. Rhee, J. Baik, and M. Choi. 2016. Downscaling of AMSR-E soil moisture with MODIS products using machine learning approaches. *Environmental Earth Sciences* 75: 12665. doi:10.1007/s12665-016-5917-6.
- Imaoka, K., M. Kachi, M. Kasahara, N. Ito, K. Nakagawa, and T. Oki. 2010. Instrument performance and calibration of AMSR-E and AMSR2. *International Archives of the Photogrammetry, Remote Sensing and Spatial Information Sciences - ISPRS Archives* 38: 13–16.
- Jackson, T. J. 1993. Microwave remote sensing. *Environmental Science and Engineering (Subseries: Environmental Science)* 7: 133–144. doi:10.1007/978-3-642-34085-7_9.
- Jackson, T. J., J. Schmugge, and E. T. Engman. 1996. Remote sensing applications to hydrology: soil moisture. *Hydrological Sciences Journal* 41: 517–530. doi:10.1080/02626669609491523.
- Jong-Sen Lee, Jen-Hung Wen, T. L. Ainsworth, Kun-Shan Chen, and A. J. Chen. 2009. Improved Sigma Filter for Speckle Filtering of SAR Imagery. *IEEE Transactions on Geoscience and Remote Sensing* 47: 202–213. doi:10.1109/TGRS.2008.2002881.
- Karjalainen, M., H. Kaartinen, J. Hyypä, H. Laurila, and R. Kuittinen. 2004. The use of Envisat alternating polarization SAR images in agricultural monitoring in comparison with radarsat-1 SAR images. *International Archives of the Photogrammetry, Remote Sensing and Spatial Information Sciences - ISPRS Archives* 35.
- Kaufman, Y. J., and C. Sendra. 1988. Algorithm for automatic atmospheric corrections to visible and near-IR satellite imagery. *International Journal of Remote Sensing* 9. Taylor & Francis: 1357–1381. doi:10.1080/01431168808954942.
- Ke, Y., J. Im, S. Park, and H. Gong. 2016. Downscaling of MODIS One kilometer evapotranspiration using Landsat-8 data and machine learning approaches. *Remote Sensing* 8: 1–26. doi:10.3390/rs8030215.
- Kerr, Y. H., P. Waldteufel, J. P. Wigneron, J. M. Martinuzzi, J. Font, and M. Berger. 2001. Soil moisture retrieval from space: The Soil Moisture and Ocean Salinity (SMOS) mission. *IEEE Transactions on Geoscience and Remote Sensing* 39: 1729–1735. doi:10.1109/36.942551.

- Kingma, D. P., and J. L. Ba. 2015. Adam: A method for stochastic optimization. *3rd International Conference on Learning Representations, ICLR 2015 - Conference Track Proceedings*: 1–15.
- Koyama, C. N., H. Liu, K. Takahashi, M. Shimada, M. Watanabe, T. Khuut, and M. Sato. 2017. In-situ measurement of soil permittivity at various depths for the calibration and validation of low-frequency SAR soil moisture models by using GPR. *Remote Sensing* 9: 1–14. doi:10.3390/rs9060580.
- Läntmateriet. 2020. GSD-Höjddata, grid 2+.
- Liang, M., and X. Hu. 2015. Recurrent convolutional neural network for object recognition. *Proceedings of the IEEE Computer Society Conference on Computer Vision and Pattern Recognition* 07-12-June: 3367–3375. doi:10.1109/CVPR.2015.7298958.
- Lievens, H., N. E. C. Verhoest, E. De Keyser, H. Vernieuwe, P. Matgen, J. Álvarez-Mozos, and B. De Baets. 2011. Effective roughness modelling as a tool for soil moisture retrieval from C- and L-band SAR. *Hydrology and Earth System Sciences* 15: 151–162. doi:10.5194/hess-15-151-2011.
- Liu, Y. Y., R. M. Parinussa, W. A. Dorigo, R. A. M. De Jeu, W. Wagner, A. I. J. M. Van Dijk, M. F. McCabe, and J. P. Evans. 2011. Developing an improved soil moisture dataset by blending passive and active microwave satellite-based retrievals. *Hydrology and Earth System Sciences* 15: 425–436. doi:10.5194/hess-15-425-2011.
- Ma, L., Y. Liu, X. Zhang, Y. Ye, G. Yin, and B. A. Johnson. 2019. Deep learning in remote sensing applications: A meta-analysis and review. *ISPRS Journal of Photogrammetry and Remote Sensing* 152. Elsevier: 166–177. doi:10.1016/j.isprsjprs.2019.04.015.
- Main-Knorn, M., B. Pflug, J. Louis, V. Debaecker, U. Müller-Wilm, and F. Gascon. 2017. Sen2Cor for Sentinel-2: 3. doi:10.1117/12.2278218.
- Malhotra, P., T. V. Vishnu, L. Vig, P. Agarwal, and G. Shroff. 2017. TimeNet: Pre-trained deep recurrent neural network for time series classification. *ESANN 2017 - Proceedings, 25th European Symposium on Artificial Neural Networks, Computational Intelligence and Machine Learning*: 607–612.
- Masrur Ahmed, A. A., R. C. Deo, N. Raj, A. Ghahramani, Q. Feng, Z. Yin, and L. Yang. 2021. Deep learning forecasts of soil moisture: Convolutional neural network and gated recurrent unit models coupled with satellite-derived modis, observations and synoptic-scale climate index data. *Remote Sensing* 13: 1–30. doi:10.3390/rs13040554.
- Mayer, B., and A. Kylling. 2005. Technical note: The libRadtran software package for radiative transfer calculations - Description and examples of use. *Atmospheric Chemistry and Physics* 5: 1855–1877. doi:10.5194/acp-5-1855-2005.
- McCulloch, W. S., and W. Pitts. 1943. A logical calculus of the ideas immanent in nervous activity. *The bulletin of mathematical biophysics* 5: 115–133. doi:10.1007/BF02478259.
- Medsker, L., S. B. Unadkat, and M. M. Ciocoiu. 2001. Applications. In *Recurrent Neural Networks Design and Applications*, ed. L. Medsker and L. C. Jain, 19–22. CRC Press LLC.
- Mikolov, T., M. Karafiát, Lukáš Burget, J. “Honza” Černocký, and S. Khudanpur. 2010. Recurrent neural network based language model. *Interspeech* 25: 1045–1048.
- Miranda, N., and P. J. Meadows. 2015. *Radiometric Calibration of S-I Level-1 Products Generated by the S-I IPF. ESA-EOPG-CSCOP-TN-0002*.
- Mittelbach, H., I. Lehner, and S. I. Seneviratne. 2012. Comparison of four soil moisture sensor types under field conditions in Switzerland. *Journal of Hydrology* 430–431. Elsevier B.V.: 39–49. doi:10.1016/j.jhydrol.2012.01.041.
- Mohanty, B. P., M. H. Cosh, V. Lakshmi, and C. Montzka. 2017. Soil Moisture Remote Sensing: State-of-the-Science. *Vadose Zone Journal* 16: vzj2016.10.0105. doi:10.2136/vzj2016.10.0105.
- Moran, M. S., D. C. Hymer, J. Qi, and E. E. Sano. 2000. Soil moisture evaluation using multi-temporal synthetic aperture radar (SAR) in semiarid rangeland. *Agricultural and Forest Meteorology* 105: 69–80. doi:10.1016/S0168-1923(00)00189-1.

- Murakami, K., and H. Taguchi. 1991. Gesture Recognition using Recurrent Neural Networks. *ACM*: 237–242. doi:10.1007/978-3-319-30973-6_9.
- National Land Survey of Finland. 2021. Elevation model 2 m. <https://www.maanmittauslaitos.fi/en/maps-and-spatial-data/expert-users/product-descriptions/elevation-model-2-m>. Accessed May 19.
- Njoku, E. G., and J. A. Kong. 1977. Theory for Passive Microwave Remote Sensing of Near-Surface Soil Moisture. *J Geophys Res* 82: 3108–3118. doi:10.1029/JB082i020p03108.
- Njoku, E. G., T. J. Jackson, V. Lakshmi, T. K. Chan, and S. V. Nghiem. 2003. Soil moisture retrieval from AMSR-E. *IEEE Transactions on Geoscience and Remote Sensing* 41. IEEE: 215–228. doi:10.1109/TGRS.2002.808243.
- Notarnicola, C., M. Angiulli, and F. Posa. 2008. Soil moisture retrieval from remotely sensed data: Neural network approach versus Bayesian method. *IEEE Transactions on Geoscience and Remote Sensing* 46: 547–557. doi:10.1109/TGRS.2007.909951.
- Owe, M., and A. A. Van De Griend. 1998. Comparison of soil moisture penetration depths for several bare soils at two microwave frequencies and implications for remote sensing. *Water Resources Research* 34: 2319–2327. doi:10.1029/98WR01469.
- Paloscia, S., S. Pettinato, E. Santi, C. Notarnicola, L. Pasolli, and A. Reppucci. 2013. Soil moisture mapping using Sentinel-1 images: Algorithm and preliminary validation. *Remote Sensing of Environment* 134. Elsevier Inc.: 234–248. doi:10.1016/j.rse.2013.02.027.
- Pariante, S. 2002. Spatial Patterns of Soil Moisture as Affected by Shrubs, in Different Climatic Conditions. *Environmental Monitoring and Assessment* 73: 237–251. doi:10.1023/A:1013119405441.
- Park, S.-E., Y. T. Jung, J.-H. Cho, H. Moon, and S. Han. 2019. Assessment of different stochastic models for inter-system bias between GPS and BDS. *Remote Sensing* 11: 1–17. doi:10.3390/rs11080894.
- Patel, P., H. S. Srivastava, S. Panigrahy, and J. S. Parihar. 2006. Comparative evaluation of the sensitivity of multi-polarized multi-frequency SAR backscatter to plant density. *International Journal of Remote Sensing* 27. Taylor & Francis: 293–305. doi:10.1080/01431160500214050.
- Peel, M. C., B. L. Finlayson, and T. A. McMahon. 2007. Updated world map of the Köppen-Geiger climate classification. *Hydrology and Earth System Sciences* 11: 1633–1644. doi:10.5194/hess-11-1633-2007.
- Pelletier, C., G. I. Webb, and F. Petitjean. 2019. Temporal Convolutional Neural Network for the Classification of Satellite Image Time Series: 1–22.
- Peng, J., C. Albergel, A. Balenzano, L. Brocca, O. Cartus, M. H. Cosh, W. T. Crow, K. Dabrowska-zielinska, et al. 2020. Remote Sensing of Environment A roadmap for high-resolution satellite soil moisture applications – confronting product characteristics with user requirements. Elsevier Inc.
- Piantanida, R., G. Hajduch, and J. Poullaouec. 2019. *Sentinel-1 Level 1 Detailed Algorithm Definition*.
- Prakash, R., D. Singh, and N. P. Pathak. 2012. A fusion approach to retrieve soil moisture with SAR and optical data. *IEEE Journal of Selected Topics in Applied Earth Observations and Remote Sensing* 5. IEEE: 196–206. doi:10.1109/JSTARS.2011.2169236.
- Qi, C., S. Huang, and X. Wang. 2020. Monitoring water quality parameters of Taihu lake based on remote sensing images and LsTM-RnN. *IEEE Access* 8: 188068–188081. doi:10.1109/ACCESS.2020.3030878.
- Rahimzadeh-Bajgiran, P., A. A. Berg, C. Champagne, and K. Omasa. 2013. Estimation of soil moisture using optical/thermal infrared remote sensing in the Canadian Prairies. *ISPRS Journal of Photogrammetry and Remote Sensing* 83. International Society for Photogrammetry and Remote Sensing, Inc. (ISPRS): 94–103. doi:10.1016/j.isprs.2013.06.004.
- Ranney, K. J., J. D. Niemann, B. M. Lehman, T. R. Green, and A. S. Jones. 2015. A method to downscale soil moisture to fine resolutions using topographic, vegetation, and soil data. *Advances*

- in Water Resources* 76. Elsevier Ltd: 81–96. doi:10.1016/j.advwatres.2014.12.003.
- Rao, B., and D. Singh. 2011. Moisture Content Determination by TDR and Capacitance Techniques: A Comparative Study. *Int. J. Earth Sci. Eng.* 4.
- Richter, R., J. Louis, and B. Berthelot. 2011. *Sentinel-2 MSI – Level 2A Products Algorithm Theoretical Basis Document*. S2PAD-ATBD-0001. European Space Agency, (Special Publication). Vol. 49.
- Robock, A., K. Y. Vinnikov, G. Srinivasan, J. K. Entin, S. E. Hollinger, N. A. Speranskaya, S. Liu, and A. Namkhai. 2000. The Global Soil Moisture Data Bank. *Bulletin of the American Meteorological Society* 81: 1281–1299. doi:10.1175/1520-0477(2000)081<1281:TGSMDB>2.3.CO;2.
- Rosenblatt, F. 1958. The perceptron: A probabilistic model for information storage and organization in the brain. *Psychological Review*. US: American Psychological Association. doi:10.1037/h0042519.
- Ruder, S. 2016. An overview of gradient descent optimization algorithms. *arXiv preprint: arXiv:1609.04747*: 1–14.
- Sadeghi, M., E. Babaieian, M. Tuller, and S. B. Jones. 2017. The optical trapezoid model: A novel approach to remote sensing of soil moisture applied to Sentinel-2 and Landsat-8 observations. *Remote Sensing of Environment* 198. Elsevier Inc.: 52–68. doi:10.1016/j.rse.2017.05.041.
- Schläpfer, D., C. C. Borel, J. Keller, and K. I. Itten. 1998. Atmospheric precorrected differential absorption technique to retrieve columnar water vapor. *Remote Sensing of Environment* 65: 353–366. doi:10.1016/S0034-4257(98)00044-3.
- Schmugge, T. 1978. Remote Sensing of Surface Soil Moisture. *Journal of Applied Meteorology* 17: 1549–1557.
- Seneviratne, S. I., T. Corti, E. L. Davin, M. Hirschi, E. B. Jaeger, I. Lehner, B. Orlowsky, and A. J. Teuling. 2010. Investigating soil moisture-climate interactions in a changing climate: A review. *Earth-Science Reviews* 99. Elsevier B.V.: 125–161. doi:10.1016/j.earscirev.2010.02.004.
- Singh, A., K. Gaurav, G. K. Meena, and S. Kumar. 2020. Estimation of soil moisture applying modified Dubois model to Sentinel-1; A regional study from Central India. *Remote Sensing* 12: 1–19. doi:10.3390/rs12142266.
- Small, D., and A. Schubert. 2008. *Guide to ASAR Geocoding*. RSL-ASAR-GC-AD.
- Smith, L. N. 2017. Cyclical learning rates for training neural networks. *Proceedings - 2017 IEEE Winter Conference on Applications of Computer Vision, WACV 2017*: 464–472. doi:10.1109/WACV.2017.58.
- State Meteorological Agency. 2021. Standard climate values.
- Styrelsen for Dataforsyning og Effektivisering. 2007. DHM-2007/Terræn.
- Su, Y., R. Liu, Y. Zhao, W. Sun, C. Niu, and D. Pei. 2019. Robust anomaly detection for multivariate time series through stochastic recurrent neural network. *Proceedings of the ACM SIGKDD International Conference on Knowledge Discovery and Data Mining* 1485: 2828–2837. doi:10.1145/3292500.3330672.
- Sun, Q., C. Miao, Q. Duan, H. Ashouri, S. Sorooshian, and K. L. Hsu. 2018. A Review of Global Precipitation Data Sets: Data Sources, Estimation, and Intercomparisons. *Reviews of Geophysics* 56: 79–107. doi:10.1002/2017RG000574.
- Susha Lekshmi, S. U., D. N. Singh, and M. Shojaei Baghini. 2014. A critical review of soil moisture measurement. *Measurement: Journal of the International Measurement Confederation* 54. Elsevier Ltd: 92–105. doi:10.1016/j.measurement.2014.04.007.
- Swedish Meteorological and Hydrological Institute. 2021a. Nederbörd.
- Swedish Meteorological and Hydrological Institute. 2021b. Temperatur.
- Visconti, F., J. M. de Paz, D. Martínez, and M. J. Molina. 2014. Laboratory and field assessment of the capacitance sensors Decagon 10HS and 5TE for estimating the water content of irrigated soils. *Agricultural Water Management* 132. Elsevier B.V.: 111–119. doi:10.1016/j.agwat.2013.10.005.

- Visin, F., K. Kastner, K. Cho, M. Matteucci, A. Courville, and Y. Bengio. 2015. ReNet: A Recurrent Neural Network Based Alternative to Convolutional Networks: 1–9.
- Wagner, W., K. Scipal, C. Pathe, D. Gerten, W. Lucht, and B. Rudolf. 2003. Evaluation of the agreement between the first global remotely sensed soil moisture data with model and precipitation data. *Journal of Geophysical Research: Atmospheres* 108. doi:10.1029/2003jd003663.
- Wan, R., S. Mei, J. Wang, M. Liu, and F. Yang. 2019. Multivariate temporal convolutional network: A deep neural networks approach for multivariate time series forecasting. *Electronics (Switzerland)* 8. doi:10.3390/electronics8080876.
- Wang, C., X.-H. Wu, L.-Q. Li, Y.-S. Wang, and Z.-W. Li. 2018. Convolutional Neural Network Application in Prediction of Soil Moisture Content. *Guang Pu Xue Yu Guang Pu Fen Xi/Spectroscopy and Spectral Analysis* 38: 36–41. doi:10.3964/j.issn.1000-0593(2018)01-0036-06.
- Wang, L., and J. J. Qu. 2009. Satellite remote sensing applications for surface soil moisture monitoring: A review. *Frontiers of Earth Science in China* 3: 237–247. doi:10.1007/s11707-009-0023-7.
- Wang, Q., S. Liu, J. Chanussot, and X. Li. 2019. Scene Classification With Recurrent Attention of VHR Remote Sensing Images. *IEEE Transactions on Geoscience and Remote Sensing* 57: 1155–1167. doi:10.1109/TGRS.2018.2864987.
- Wang, S., B. J. Fu, G. Y. Gao, X. L. Yao, and J. Zhou. 2012. Soil moisture and evapotranspiration of different land cover types in the Loess Plateau, China. *Hydrology and Earth System Sciences* 16: 2883–2892. doi:10.5194/hess-16-2883-2012.
- Wei, Z., Y. Meng, W. Zhang, J. Peng, and L. Meng. 2019. Downscaling SMAP soil moisture estimation with gradient boosting decision tree regression over the Tibetan Plateau. *Remote Sensing of Environment* 225. Elsevier: 30–44. doi:10.1016/j.rse.2019.02.022.
- Xing, C., N. Chen, X. Zhang, and J. Gong. 2017. A machine learning based reconstruction method for satellite remote sensing of soil moisture images with in situ observations. *Remote Sensing* 9. doi:10.3390/rs9050484.
- Zhang, D., and G. Zhou. 2016. Estimation of soil moisture from optical and thermal remote sensing: A review. *Sensors (Switzerland)* 16. doi:10.3390/s16081308.

Appendix A: Data specifications

Table A1: Descriptions of datasets used in this study and the variables derived from them.

Product	Name	Region / Probe network	Source	Method	Resolution (temporal / spatial)	Accuracy (vertical / horizontal)	Year of production (start)
SSM	HOBE	Denmark / HOBE	ISMN (Dorigo et al. 2011; Dorigo et al. 2013)	In situ	1 hour / -	-	
SSM	FMI	Finland / FMI	ISMN (Dorigo et al. 2011; Dorigo et al. 2013)	In situ	1 hour / -	-	
SSM	REMEDIHUS	Spain / REMEDIHUS	ISMN (Dorigo et al. 2011; Dorigo et al. 2013)	In situ	1 hour / -	-	
SSM	ICOS	Sweden / ICOS	ICOS	In situ	30 minutes / -	-	
TS	HOBE	Denmark / HOBE	ISMN (Dorigo et al. 2011; Dorigo et al. 2013)	In situ	1 hour	-	
TS	FMI	Finland / FMI	ISMN (Dorigo et al. 2011; Dorigo et al. 2013)	In situ	1 hour	-	
TS	REMEDIHUS	Spain / REMEDIHUS	ISMN (Dorigo et al. 2011; Dorigo et al. 2013)	In situ	1 hour	-	
TS	ICOS	Sweden / ICOS	ICOS	In situ	30 minutes	-	
TA / Precipitation	HOBE	Denmark / HOBE	Danish Meteorological Institute (2016)	In situ	Daily	-	
TA / Precipitation	FMI	Finland / FMI	Finnish Meteorological Institute (2021)	In situ	6 hours	-	
TA / Precipitation	REMEDIHUS	Spain / REMEDIHUS	AEMET (2021)	In situ	Daily	-	

TA / Precipitation	ICOS, Temperatur, Nederbörd	Sweden / ICOS	ICOS, Swedish Meteorological and Hydrological Institute (2021a); Swedish Meteorological and Hydrological Institute (2021b)	In situ	30-60 minutes	-	
DTM	DHM-2007/Terræn	Denmark / HOBE	Styrelsen for Dataforsyning og Effektivisering (2007)	Remote sensing	1.6 m	0.05 m / 0.15 m	2007
DTM	Elevation model 2 m	Finland / FMI	National Land Survey of Finland (2021)	Remote sensing	2 m	0.3 m / 0.3 m	Updated monthly
DTM	MDT05	Spain / REMEDHUS	Centro Nacional de Información Geográfica (2021)	Remote sensing	5 m	- / -	2018
DTM	GSD-Höjddata, grid 2+	Sweden / ICOS	Läntmateriet (2020)	Remote sensing	2 m	- / -	2019
Soil map	HWSD v1.2	Global	Fischer et al. (2008)	Various	30 arc-seconds	- / -	1974-1990
Land cover	CLC2018	European	European Environmental Agency (2018)	In situ, remote sensing	100 m	- / 100 m	2018
Sigma nought (σ^0)	Sentinel-1 GRD interferometric wide swath	Global	Copernicus (ESA)	Remote sensing	10 m	- / -	-
NDVI / NDWI	Sentinel-2 L2A	Global	Copernicus (ESA)	Remote sensing	10-20 m	- / -	-
ECV_SM v5.2	Essential Climate Variables for Soil Moisture	Global	ESA (Liu et al. 2011; Dorigo et al. 2015; Dorigo et al. 2017)	Remote sensing	25 arc-seconds	-	2020
CSM	Copernicus Soil Moisture	European	Copernicus (ESA) (Bauer- Marschallinger et al. 2019)	Remote sensing	1 km	-	2015

Table A2: Model variables and classifications of their type and resampling method (if applicable).

Variable	Resampling	Unit	Dimensions	Type
Surface soil moisture (SSM)	Daily mean	Percent	Temporal	Dynamic
Soil temperature (TS_{max})	Daily max	Degrees Celcius	Temporal	Dynamic
Sigma nought (σ^0)	-	-	Spatio-temporal	Dynamic
Normalized difference vegetation index (NDVI)	-	-	Spatio-temporal	Dynamic
Normalized difference water index (NDWI)	-	-	Spatio-temporal	Dynamic
Precipitation	Daily sum	mm	Temporal	Dynamic
Consecutive dry days	-	Days	Temporal	Dynamic
Air temperature (TA_{max})	Daily max	Degrees Celcius	Temporal	Dynamic
Air temperature (TA_{mean})	Daily mean	Degrees Celcius	Temporal	Dynamic
Air temperature (TA_{min})	Daily min	Degrees Celcius	Temporal	Dynamic
Elevation	-	Meters above sea level	Spatial	Static
Slope	-	%	Spatial	Static
Aspect _x	-	Degrees	Spatial	Static
Aspect _y	-	Degrees	Spatial	Static
Land cover	-	Nominal	Spatial	Static
Base saturation	-	%	Point-based	Static
Clay fraction	-	%	Point-based	Static
Silt fraction	-	%	Point-based	Static
Sand fraction	-	%	Point-based	Static
Organic carbon	-	%	Point-based	Static

Appendix B: Model and Soil Moisture Products Predictions

Table B1. Probe-specific mean absolute errors (MAE) for the deep learning model (DLM) and soil moisture (SM) products, ECV_SM and CSM.

ID	Model (full)	Model (minimum)	Model (agriculture)	CSM	ECV_SM	CLC	Probe network
1.01	0.0581	0.0638		0.2639	0.0833	Moors and heathland	HOBE
1.03	0.0385	0.0788		0.3045	0.0659	Moors and heathland	HOBE
1.04	0.2449	0.22		0.2057	0.2244	Coniferous forest	HOBE
1.05	0.053	0.0943		0.3203	0.0677	Coniferous forest	HOBE
1.06	0.0618	0.0311	0.0365	0.2854	0.0533	Non-irrigated arable land	HOBE
1.07	0.0791	0.0568		0.3003	0.0637	Complex cultivation pattern	HOBE
1.08	0.0373	0.0497	0.0444	0.276	0.0466	Non-irrigated arable land	HOBE
1.09	0.0508	0.05	0.045	0.3113	0.0591	Non-irrigated arable land	HOBE
1.1	0.0853	0.0753	0.0653	0.3875	0.1054	Non-irrigated arable land	HOBE
2.01	0.1355	0.0321		0.3327	0.0719	Coniferous forest	HOBE
2.03	0.0539	0.0433	0.0334	0.3843	0.0648	Non-irrigated arable land	HOBE
2.04	0.0446	0.064	0.0503	0.3175	0.0481	Non-irrigated arable land	HOBE
2.05	0.0713	0.0449	0.0604	0.3104	0.0553	Non-irrigated arable land	HOBE
2.06	0.0589	0.0446		0.385	0.0944	Land principally occupied by agriculture	HOBE
2.07	0.0476	0.0563	0.0654	0.3532	0.0716	Non-irrigated arable land	HOBE
2.08	0.1325	0.0776	0.0951	0.2546	0.0936	Non-irrigated arable land	HOBE
2.09	0.3515	0.3167	0.3202	0.2418	0.2833	Non-irrigated arable land	HOBE
2.1	0.0715	0.0734		0.2657	0.0655	Beaches, dunes, sands	HOBE
2.11	0.1831	0.1398		0.2592	0.1677	Moors and heathland	HOBE
3.01	0.0503	0.0553	0.0611	0.3459	0.0576	Non-irrigated arable land	HOBE
3.02	0.0557	0.0423	0.0504	0.3115	0.0583	Non-irrigated arable land	HOBE
3.03	0.0628	0.0433	0.0643	0.4947	0.0965	Non-irrigated arable land	HOBE

3.04	0.0405	0.0424	0.0455	0.2853	0.0589	Non-irrigated arable land	HOBE
3.05	0.0551	0.0499		0.3547	0.0627	Land principally occupied by agriculture	HOBE
3.06	0.1694	0.1258		0.3882	0.1305	Coniferous forest	HOBE
3.07	0.1273	0.0798	0.0856	0.2946	0.0861	Non-irrigated arable land	HOBE
3.08	0.0296	0.0527	0.0455	0.2966	0.0539	Non-irrigated arable land	HOBE
3.09	0.0609	0.049		0.3175	0.0632	Land principally occupied by agriculture	HOBE
Canizal	0.1664	0.1175	0.0804	0.2611	0.0496	Permanently irrigated field	REMEDHUS
Carretoro	0.0475	0.0927	0.0707	0.4111	0.1576	Non-irrigated arable land	REMEDHUS
Casa_Periles	0.041	0.0321	0.0461	0.3458	0.0893	Non-irrigated arable land	REMEDHUS
Concejo_del_Monte	0.0593	0.0729	0.0782	0.2932	0.0415	Non-irrigated arable land	REMEDHUS
El_Coto	0.0466	0.0692	0.0817	0.4359	0.1805	Non-irrigated arable land	REMEDHUS
El_Tomillar	0.1082	0.0527		0.4533	0.1890	Vineyards	REMEDHUS
Granja_g	0.0515	0.0459	0.0569	0.3792	0.1227	Permanently irrigated field	REMEDHUS
Guarrati	0.2465	0.1103		0.2496	0.0794	Natural grasslands	REMEDHUS
La_Atalaya	0.0446	0.0399	0.0489	0.3365	0.1104	Non-irrigated arable land	REMEDHUS
La_Cruz_de_Elias	0.0291	0.0412	0.0474	0.3212	0.0625	Non-irrigated arable land	REMEDHUS
Las_Arenas	0.0697	0.0764	0.0805	0.3029	0.0480	Non-irrigated arable land	REMEDHUS
Las_Bodegas	0.043	0.0458	0.0351	0.3339	0.0595	Non-irrigated arable land	REMEDHUS
Las_Brozas	0.0706	0.0312		0.384	0.1187	Vineyards	REMEDHUS
Las_Eritas	0.2094	0.1566	0.171	0.238	0.0637	Non-irrigated arable land	REMEDHUS
Las_Tres_Rayas	0.0822	0.0405	0.0379	0.3633	0.1051	Non-irrigated arable land	REMEDHUS
Las_Vacas	0.0307	0.0389	0.0383	0.3914	0.1378	Permanently irrigated field	REMEDHUS
Las_Victorias	0.1538	0.0794	0.0994	0.447	0.1881	Non-irrigated arable land	REMEDHUS
Llanos_de_la_Boveda	0.103	0.0573	0.0703	0.2953	0.0375	Non-irrigated arable land	REMEDHUS
Paredinas	0.0645	0.0656		0.4477	0.1876	Vineyards	REMEDHUS
Zamarron	0.0249	0.0461	0.0325	0.3853	0.1309	Non-irrigated arable land	REMEDHUS

SOD011	0.2433	0.1309		0.3969	0.0999	Coniferous forest	FMI
SOD021	0.6056	0.5409		0.3901	0.6550	Peat bogs	FMI
SOD071	0.0686	0.0725		0.2363	0.1031	Coniferous forest	FMI
SOD081	0.1936	0.0774		0.3216	0.0654	Coniferous forest	FMI
SOD091	0.5435	0.4835		0.3106	0.4786	Coniferous forest	FMI
SOD101	0.0897	0.0747		0.2823	0.0848	Coniferous forest	FMI
SOD130	0.149	0.0423		0.2592	0.0584	Coniferous forest	FMI
SOD140	0.128	0.1784		0.274	0.0677	Beaches, dunes, sands	FMI
Degero	0.2969	0.2068		0.1982	0.3094	Peat bogs	ICOS
Hyltemossa	0.1159	0.1029		0.246	0.1266	Coniferous forest	ICOS
Lanna	0.1344	0.0728	0.0634	0.2794	0.0688	Non-irrigated arable land	ICOS
Norunda	0.0652	0.0795		0.3211	0.0760	Coniferous forest	ICOS
Stordalen	0.1769	0.1592		0.1271	0.2218	Peat bogs	ICOS